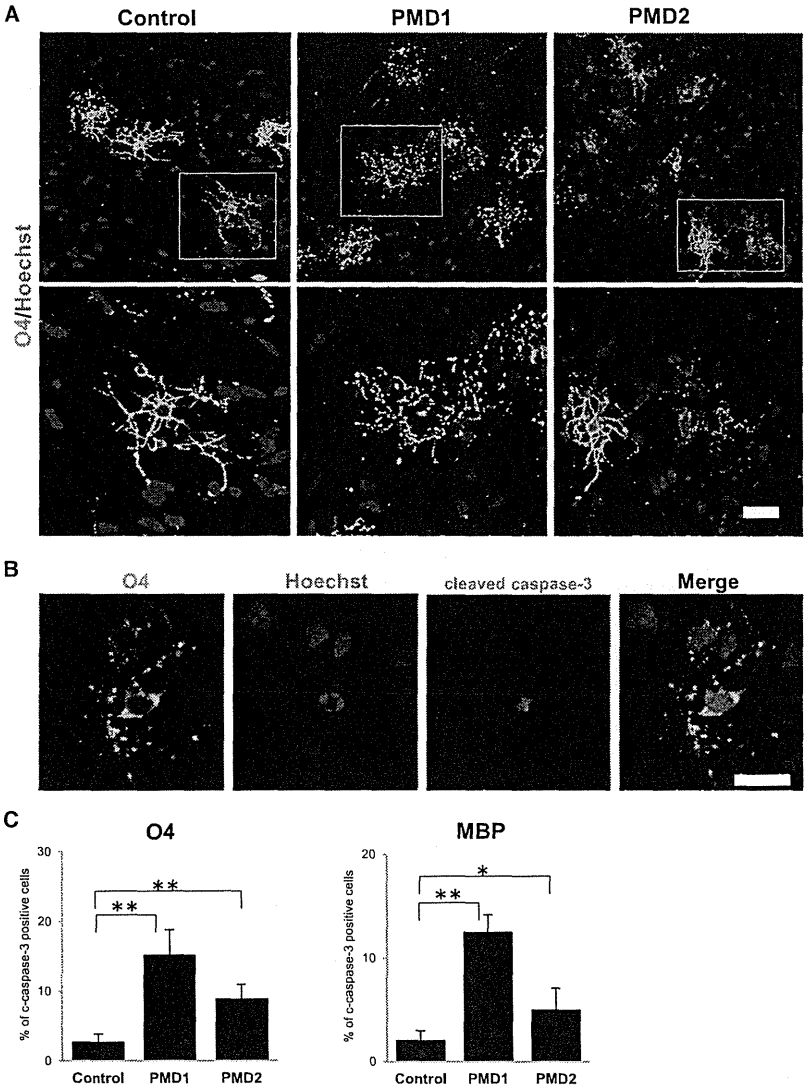

Figure 5. Enhanced Apoptosis in PMD iPSC-Derived Oligodendrocytes

(A) Morphological differences in OLs. Immunocytochemical analysis of iPSC-derived OLs for OLs marker (O4) and nuclei (Hoechst). The OLs showed a uniform appearance in the control iPSC-derived cells but showed scattered morphologies in the PMD iPSC-derived cells. The scale bar represents 40 μm.

(B) Representative immunocytochemical images of apoptotic OLs using markers for apoptosis (cleaved caspase-3) and OLs (O4). OLs ($O4^+$ or MBP^+) that were both positive for cleaved caspase-3 and showed nuclear condensation or fragmentation were considered apoptotic OLs. The scale bar represents 40 μm. c-caspase-3, cleaved caspase-3.

(C) Quantitative analysis of the number of apoptotic OLs. The number of apoptotic cells was higher in the PMD1 (PMD1-7, PMD1-15, and PMD1-27) and PMD2 iPSC (PMD2-6, PMD2-10, and PMD2-22)-derived OLs than control iPSC (201B7, WD39, and TIG121)-derived OLs (n = 9; mean ± SEM; independent experiments; *p < 0.05; **p < 0.01; Mann-Whitney's U test).

2006), we next investigated whether apoptosis was induced in PMD patient-derived neurons. However, no cleaved caspase-3^+ neurons derived from either control or PMD iPSCs were observed (Figure S2C), suggesting that this increased apoptosis was specific to oligodendrocyte lineage cells in PMD in our iPSC-derived cultures.

Abnormal Myelin Structures and ER Morphologies Were Detected by Electron Microscopic Analysis

Finally, we focused on the myelinating properties of PMD iPSC-derived OLs, which represent the most characteristic pathogenic feature of PMD. Because different types of neural cells, including neurons and astrocytes, in addition to OLs, were derived in our cultures, neuron-glial interactions could be observed and neuron myelination by the iPSC-derived OLs could be analyzed in situ. In immunocytochemical analysis of MBP and NF200 (neurofilament marker), parts of the neurofilament$^+$ neurites were wrapped by the MBP^+ process of iPSC-derived oligodendrocytes (Figure S3A). Thus, to evaluate the histological abnormality of the myelin structures in vitro, we performed transmission electron microscopy (TEM) analysis of ultrathin sections of the differentiated cells. The results showed that myelin structures with or without axons could be observed via TEM. Considering the neuronal processes wrapped by the MBP^+ process of iPSC-derived OLs observed through immunocytochemistry, some of the axonal structures could have been lost during the fixation process for TEM.

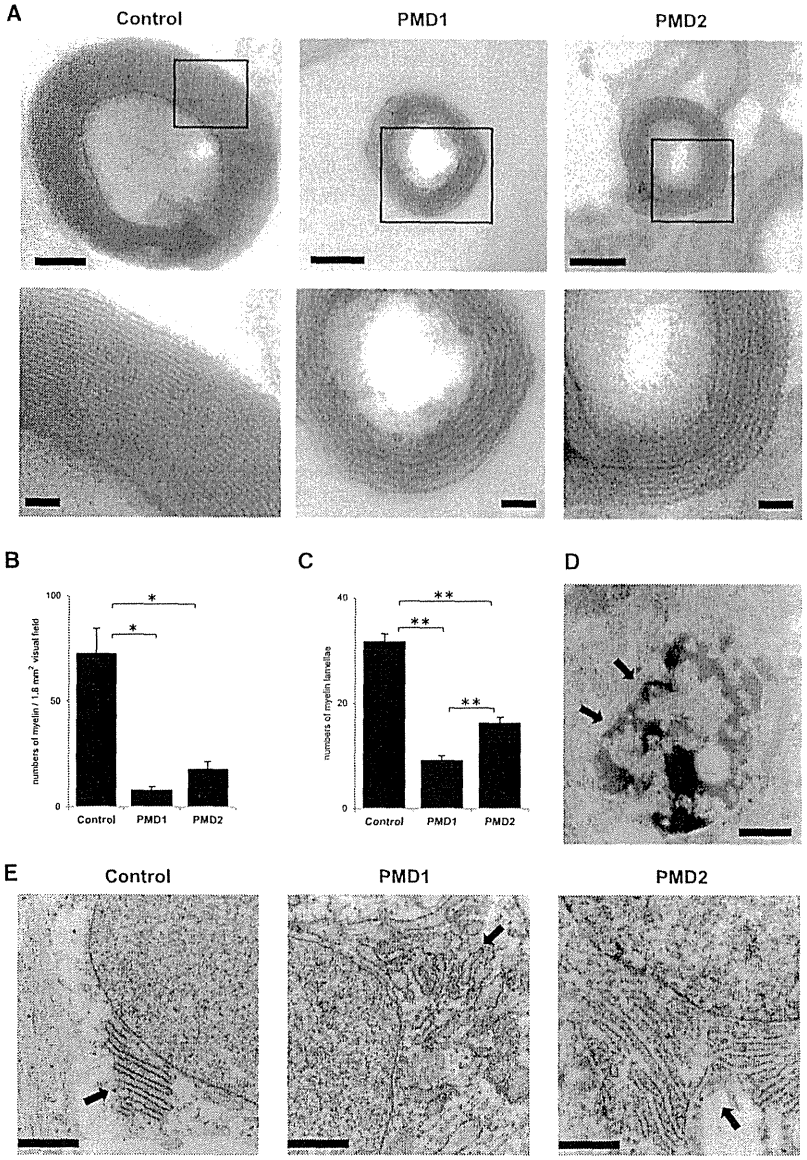

Figure 6. Electron Microscopic Analysis of PMD iPSC-Derived Cells

(A) TEM of iPSC-derived cells. The maximum number of normal myelin lamella was greater than 30 in the control iPSC-derived myelin sheaths. In contrast, a limited number of myelin lamella was observed in the PMD iPSC-derived myelin sheaths. High-magnification images are also shown in the lower panel. The scale bars represent 100 nm (upper panels) and 20 nm (lower panels).

(B) Quantitative analysis of the numbers of myelin structures. We counted the numbers of myelin structures per visual field of EM images (approximately 1.8 mm^2) for the myelination frequency. The frequency of myelin formation was significantly decreased in both PMD1 (PMD1-7, PMD1-15, and PMD1-27) and PMD2 (PMD2-6, PMD2-10, and PMD2-22) iPSC-derived OLs (n = 3; mean ± SEM; independent experiments; *p < 0.05; t test).

(C) Quantitative analysis of the numbers of myelin lamellae. We counted the numbers of major dense lines per myelinated fiber for the thickness of myelin, and the average of the numbers of myelin lamellae in the top ten myelin sheaths are presented. The thickness of the myelin sheath was greatly reduced in both PMD1 (PMD1-7, PMD1-15, and PMD1-27) and PMD2 (PMD2-6, PMD2-10, and PMD2-22) iPSC-derived OLs (n = 3; mean ± SEM; independent experiments; **p < 0.01; t test).

(D and E) Histological abnormalities detected in PMD iPSC-derived cells via TEM. Apoptotic cells with fragmented nuclei (arrow in D) were frequently detected among the PMD-iPSC-derived cells (D). The scale bar represents 1 μm. Dilations of ER intermembrane spaces were also observed (E). The scale bars represent 0.5 μm.

Although we stained with antibodies against NAV1.6 (nodes) and CASPER (paranodes), we could not detect any significant staining in our cultures. This may suggest immature myelination in the present culture conditions.

Notably, mature myelin structures with thick myelin lamella ~30 layers were observed in the control cultures. In contrast, in the PMD iPSC-derived cultures, a limited number of myelin structures with thin myelin lamella ~15 layers were observed (Figure 6A). The frequency of myelin formation and thickness of the myelin sheath were significantly decreased in both PMD1 and PMD2 iPSC-derived OLs (Figures 6B and 6C).

In addition, several types of histological abnormalities were detected in the PMD cells. Apoptotic cells exhibiting nuclear condensation were frequently observed among the PMD iPSC-derived cells, in contrast to that observed in those derived from control iPSCs (Figure 6D). Moreover, aberrant ER morphologies, such as dilation of the ER intermembrane space (Fan et al., 2013; Lim et al., 2011), were found in the PMD iPSC-derived cells (Figure 6E). These results indicate that PMD iPSC-derived OLs develop a poor myelin structure and subsequently die, supporting the involvement of ER stress in the pathogenesis of PMD.

DISCUSSION

In this study, we established PMD-specific human iPSCs from two patients with different clinical severity and different missense mutations of *PLP1*. One mutation is in the transmembrane domain (PMD1) and the other is in the extracellular domain (PMD2), both of which differ from those in the previously reported PMD animal models. And we generated patient-specific OLs. This model enables an investigation of the correlations between the molecular pathophysiology of PMD and various cell biological phenomena, including OL differentiation, myelination, and apoptosis in patient-derived live OLs through morphological, biochemical, and molecular biological methods. These analyses could not be achieved using conventional disease models.

Although there are several reported methods for inducing OPCs from human ESCs (Hu et al., 2009; Izrael et al., 2007; Kang et al., 2007), these methods have difficulties in reproducibility, making it difficult to obtain sufficient amounts of mature OLs for analysis. In the present study, we developed an improved neural differentiation protocol for human pluripotent stem cells by utilizing an EB-neurosphere method involving dual Smad inhibition in combination with a GSK3 inhibitor to facilitate differentiation into NS/PCs more efficiently and reproducibly. In addition, the use of T3, ciliary neurotrophic factor (CNTF), and leukemia inhibitory factor (LIF) was beneficial for differentiation into OLs. Using this method, we achieved stable differentiation of several human iPSC clones into OLs in a similar manner to that reported in a recent study (Wang et al., 2013). Remarkably, our culture procedure enabled recapitulation of myelin formation in human iPSC (hiPSC)-derived neurites and OLs in vitro in a single-culture system without coculturing with other cells, such as rodent hippocampal neurons, as previously reported (Kang et al., 2007). Thus, this study reports a successful in vitro myelination assay using human iPSC-derived neurons and OLs.

Another important finding of this study was that the differentiation of PMD iPSCs into OLs well-recapitulated the progression of PMD pathogenesis in vitro. Although the PMD-specific iPSCs induced abundant MBP^+ mature OLs, myelination was substantially less frequent and limited lamella formation was observed. These results suggest that incomplete maturation and limited survival of OLs rather than a failure to differentiate into OLs is responsible for PMD pathogenesis. However, the cause of OL degeneration and dysmyelination observed in PMD is unclear. Some previous reports have demonstrated the involvement of ER stress in the pathogenesis of PMD associated with missense mutations in the *PLP1* gene. Analyses using cell lines, such as cos7 cells transfected with wild-type or mutant *PLP1* genes, have shown that wild-type PLP1 protein is synthesized in the ER and transported to the cell surface, whereas mutant PLP1 proteins are arrested in the secretory pathway at an early stage and accumulate in the ER (Gow et al., 1994). In the CNS of PMD model mice, such as msd and rsh mice, mutant PLP1 proteins are largely confined to the perinuclear region of OLs and involved in the UPR (Gow et al., 1998). These reports suggest the involvement of ER stress in PMD pathogenesis. In the present study, accumulation of misfolded mutant PLP1 proteins in the ER and high susceptibility to ER stresses in the PMD1 and PMD2 cells were observed. This increased susceptibility to ER stresses or other cellular response could have resulted in the apoptosis of PMD iPSC-derived OLs and immature/incomplete myelination.

In addition, we detected differences between PMD1 and PMD2 cells. The differences of susceptibility to ER stresses and the thickness of the myelin sheath were consistent with the different levels of clinical severity of the two patients. The correlations between different clinical severity, different missense mutations, and different pathogenic changes have not previously been reported by conventional disease models. These results suggest that this PMD model accurately recapitulates disease pathophysiology not only qualitatively but also in terms of the degree of disease progression, although how the different point mutations affect the degree of the observed phenotype must be clarified. Accordingly, we propose models for a "proof-of-concept" of PMD pathogenesis based on the endogenous mutations found in PMD iPSC-derived OLs. The present findings cannot be generalized to PMD as a whole because the more common *PLP1* duplication was not included; therefore, we will investigate the pathogenesis of PMD with *PLP1* duplications in the future.

The current study represents the a demonstration of pathogenic changes in PMD patients with *PLP1* missense mutations using disease-specific, human iPSC-derived OLs. This model faithfully reproduces the pathophysiology observed in the CNS of PMD patients, which is difficult to identify through conventional experiments. Moreover, our results demonstrate the usefulness of iPSC-derived OLs for the analysis of the pathogenic processes of dysmyelinating human neurological disorders and the development of novel therapeutic agents for their treatment.

EXPERIMENTAL PROCEDURES

Isolation of Human Skin Fibroblasts and Generation of iPSCs

HDFs from the dermis of a 1-year-old Japanese male patient and HDFs from the dermis of a 20-year-old Caucasian male patient (Coriell Institute: GM09546) were used to establish PMD1-iPSCs (PMD1-7, 1-15, and 1-27) and PMD2-iPSCs (PMD2-6, 2-10, and

2-22), respectively. Additional control cell lines used in this study included 201B7 (control A, established from HDFs [Cell Applications] from the dermis of a 36-year-old Caucasian female; Takahashi et al., 2007), WD39 (control B, established from HDFs from the dermis of a 16-year-old Japanese female; Imaizumi et al., 2012), and TIG121 (control C, established from HDFs from the dermis of an 8-month-old Japanese male [Japan Health Sciences Foundation]). All of the human iPSC clones were established through the retroviral transduction of four transcription factors (*SOX2*, *OCT4*, *KLF4*, and *c-MYC*) into HDFs as described previously (Takahashi et al., 2007) and evaluated based on the expression of pluripotent markers, the silencing of retroviral transgenes, and teratoma formation assays as described previously (Ohta et al., 2011). We used three clones for each group for further analysis: control (201B7, WD39, and TIG121), PMD1 (1-7, 1-15, and 1-27), and PMD2 (2-6, 2-10, and 2-22). The data from the three clones were combined in each figure, and the data are shown as the average of the three clones. All of the experimental procedures for iPSC production were approved by the ethics committee of the Keio University School of Medicine (approval number: 20-16-18).

Culture and In Vitro Differentiation of Human iPSCs

hiPSCs were grown on mitomycin-C-treated SNL murine fibroblast feeder cells in gelatin-coated (0.1%) tissue culture dishes. The hiPSCs were maintained in standard hESC medium (Dulbecco's modified Eagle's medium [DMEM]/F12 [Sigma] containing 20% KnockOut serum replacement [KSR; Life Technologies], nonessential amino acids [NEAA], 0.1 mM 2-mercaptoethanol [Sigma], and 4 ng/ml fibroblast growth factor 2 [FGF-2] [PeproTech]) at 37°C in a humidified atmosphere of 3% CO_2.

For in vitro differentiation, iPSC colonies were detached from the feeder layers en bloc using a dissociation solution (0.25% trypsin, 100 μg/ml collagenase IV [Invitrogen], 1 mM $CaCl_2$, and 20% KSR; day 0) and cultured in suspension in bacteriological dishes to form EBs in a humidified atmosphere of 3% CO_2. From day 1 to 4 of EB formation, 3 μM dorsomorphin (Sigma), 3 μM SB431542 (Tocris Bioscience), and 3 μM BIO ((2′Z, 3′E)-6-bromoindirubin-3′-oxime; Sigma) were added. In addition, 1 μM retinoic acid (Sigma) and 1 μM purmorphamine (Calbiochem) were added on days 4 and 7, respectively, and maintained thereafter until day 16 (EB dissociation). The medium was changed every 2 days. On day 16, the EBs were enzymatically dissociated into single cells using TrypLE Select (Life Technologies), and the dissociated cells were cultured in suspension at a density of 1×10^5 cells/ml in proliferation medium consisting of serum-free medium (media hormone mix [MHM]; Okada et al., 2008) supplemented with 2% B27 supplement (Invitrogen), NEAA, 1 μM purmorphamine, 60 ng/ml T3 (Sigma), 10 ng/ml PDGF-AA (PeproTech), 20 ng/ml FGF, 10 ng/ml epidermal growth factor (PeproTech), 10 ng/ml insulin growth factor 1, and 10 ng/ml neurotrophin-3 (R&D Systems) in a humidified atmosphere of 5% CO_2. The medium was changed every 4~6 days for approximately 15~20 days to form the first neurospheres. To passage neurospheres, the first neurospheres were dissociated in the same manner as described above and cultured at a density of 1×10^5 cells/ml in proliferation medium without purmorphamine for approximately 15~20 days. To assay neurosphere differentiation, undissociated 5–7 neurospheres were plated onto coverslips 10 mm in diameter coated with poly-L-ornithine (Sigma) and growth-factor-reduced Matrigel (50× dilution, thin coated; Invitrogen), and cultured in differentiation medium that consisted of MHM supplemented with 2% B27 supplement, NEAA, 60 ng/ml T3, 10 ng/ml hLIF (Millipore), and 25 ng/ml CNTF (R&D Systems) for 2–6 weeks in a humidified atmosphere of 5% CO_2. Half of the medium was changed every 2 or 3 days. For the quantitative analysis of the differentiation efficiency into OL lineage cells, the numbers of neurosphere colonies containing more than 40 marker-positive cells (≥ 40 cells, oligodendrocyte [++]), those containing less than 40 marker-positive cells (1–39 cells, oligodendrocyte [+]), and those without marker-positive cells (oligodendrocyte [−]) were counted and are presented as the percentage of total neurosphere colonies. To examine the expression of ER-stress markers, $O4^+$ differentiated cells were purified 4 weeks after the attachment of the neurospheres using MACS technology with an anti-O4 antibody.

Direct Sequencing and Pyrosequencing Analysis of the *PLP1* Gene

Genomic DNA was extracted from peripheral blood samples (leukocytes) from PMD1 and from HDFs and iPSCs from both PMD1 and PMD2. For direct sequencing of the mutations in the *PLP1* gene in PMD1, fragments of the promoter regions (5′ UTR) and all seven exons of the *PLP1* gene were amplified via PCR. The PCR primers and cycling conditions employed for direct sequencing are listed in Table S1. For pyrosequencing analysis of the mutations in the *PLP1* gene in HDFs and iPSCs, fragments containing the PMD1 mutation (c.757 T > A in exon 6) and PMD2 mutation (c.643 C > T in exon 5) were amplified via PCR using forward primers and biotinylated reverse primers. Pyrosequencing analyses were performed following the manufacturer's instructions (Pyromark Q24; QIAGEN). The PCR primers and cycling conditions applied for pyrosequencing analysis are listed in Table S2.

RNA Isolation and RT-PCR

RNA isolation and real-time quantitative RT-PCR were performed as previously described using SYBR Premix ExTaq II and the MX3000P Real-Time PCR system (Stratagene; Okada et al., 2004, 2008). The amount of cDNA was normalized to that of human-specific *β-ACTIN* mRNA.

For the analysis of the expression of retroviral transgene in iPSCs, HDFs 7 days after the retroviral introduction (day 11 of the protocol) of four genes (*SOX2*, *OCT4*, *KLF4*, and *c-MYC*) were used as the positive control (*SOX2* tg, *OCT4* tg, *KLF4* tg, and *c-MYC* tg). The data are presented as the copy numbers of mRNA for each transgene. As for the analyses of *NANOG*, *SOX1*, *BRACHYURY*, *SOX17*, *βIII tubulin*, *GFAP*, *CNP*, and ER stress marker (*BIP*, *CHOP*, and *spliced XBP1*), data are presented as the relative expression to that in control. The applied primer sequences and PCR cycling conditions are listed in Table S3.

Immunocytochemical Analysis

For immunocytochemical analysis, cells were fixed with 4% paraformaldehyde for 30 min at room temperature. After blocking in

blocking buffer (PBS containing 10% normal goat or donkey serum and 0.3% Triton X-100) for 1 hr at room temperature, the cells were incubated with primary antibodies at 4°C overnight. For O4 staining, we used blocking buffer without Triton X-100. After three washes with PBS, the cells were incubated with Alexa 488-, Alexa 555-, or Alexa 647-conjugated secondary antibodies (Life Technologies) for 1 hr at RT. Nuclei were stained with 10 μg/ml Hoechst 33258 (Sigma). After washing with PBS, the cells were mounted on slides and examined with a universal fluorescence microscope (Axiophoto; Carl Zeiss) or confocal laser scanning microscope (LSM700; Carl Zeiss). The primary antibodies used in these analyses were as follows: NANOG (1:100; ReproCELL), OCT4 (1:500; Santa Cruz Biotechnology), OLIG2 (1:1,000; R&D Systems), PDGFRα (1:2,000; Santa Cruz Biotechnology), NG2 (1:2,000; Millipore), O4 (1:5,000; Millipore), MBP (1:1,000; Serotec), β-III-tubulin (1:1,000; Sigma), NF200 (1:1,000, Millipore), GFAP (1:4,000, Dako), KDEL (Abcam), PLP1 (1:30,000; gifted from Masayuki Itoh [National Center of Neurology and Psychiatry] recognizes PLP1, but not DM20), KI67 (1:10,000, Abcam), and cleaved caspase 3 (1:1,000, Cell Signaling Technology).

Teratoma Assay

Undifferentiated iPSCs (5×10^5 cells) were injected into the testes of 8-week-old male nonobese diabetic (NOD)/severe combined immunodeficiency (SCID) mice (Charles River Laboratories) as described previously (Ohta et al., 2011). Eight weeks after injection, the resultant tumors were dissected and fixed with 4% paraformaldehyde. Paraffin-embedded tissue sections were produced, and hematoxylin and eosin (H&E) staining was performed. Images were obtained using a BZ-9000 microscope (Keyence).

Transmission Electron Microscopy

For TEM analysis, neurospheres and cells in dishes were fixed with 2.5% glutaraldehyde in 50 mM phosphate buffer (PB) overnight at 4°C. After washing twice in 0.1 M PB, these samples fixed with 1% osmium tetroxide for 90 min, dehydrated through ethanol, and embedded in Epon. The neurospheres were dissected and fixed on the stage, followed by the preparation of ultrathin sections with a thickness of 70 nm using an ultramicrotome (Leica Microsystems). The sections were subsequently stained with uranyl acetate and lead citrate for 10 and 12 min, respectively. Finally, the sections were observed under a transmission electron microscope (JEOL model 1230), and images were captured with Digital Micrograph 3.3 (Gatan). For the quantitative analysis of myelination, the number of myelin lamellae, which is the number of major dense lines per myelinated fibers, was counted to assess myelin thickness and the number of myelinated fibers per visual field of electron microscopy (EM) images (approximately 1.8 mm^2) was counted to assess myelination frequency.

SUPPLEMENTAL INFORMATION

Supplemental Information includes three figures and three tables and can be found with this article online at http://dx.doi.org/10.1016/j.stemcr.2014.03.007.

ACKNOWLEDGMENTS

We are grateful to Prof. F. Urano (Washington University School of Medicine) for valuable comments and analysis of ER stress, Prof. M. Amagai (Keio University) for skin biopsies, I. Kuki (Osaka City General Hospital) for providing patient medical information, M. Itoh (National Center of Neurology and Psychiatry) for providing PLP1 antibody, T. Nagai (Keio University) for assistance with the TEM analyses, N. Kuzumaki (Keio University) for technical assistance, and all of the members of H.O.'s laboratory for their encouragement and support. This work was supported by funding from the Project for the Realization of Regenerative Medicine and Support for Core Institutes for iPS Cell Research from the Ministry of Education, Culture; Support for the Core Institutes for iPS Cell Research from the Ministry of Education, Culture, Sports, Science and Technology of Japan (MEXT; to H.O.); and a Grant-in-Aid for the Global COE Program from MEXT to Keio University. This work was also supported by a Grant-in-Aid for Young Scientists (B) from MEXT, a Keio University Grant-in-Aid for the Encouragement of Young Medical Scientists to Y.K.-N. from the Kanrinmaru-Project at Keio University, a Grant-in-Aid for Young Scientists (A) and a Grant-in-Aid for Scientific Research on Innovative Areas (Foundation of Synapse Neurocircuit Pathology) from MEXT, and JST-CIRM Collaborative Research Program funding awarded to Y.O. H.O. is a scientific consultant for SanBio, Inc., Eisai, Co., Ltd., and Daiichi Sankyo, Co., Ltd. M.S. and A.N. are employed by Takeda Pharmaceutical Company Limited. S.Y. is a member without salary of the scientific advisory boards of iPierian, iPS Academia Japan, Megakaryon Corporation, and HEALIOS K. K. Japan.

Received: October 8, 2013
Revised: March 20, 2014
Accepted: March 20, 2014
Published: April 24, 2014

REFERENCES

Fan, J., Long, H., Li, Y., Liu, Y., Zhou, W., Li, Q., Yin, G., Zhang, N., and Cai, W. (2013). Edaravone protects against glutamate-induced PERK/EIF2α/ATF4 integrated stress response and activation of caspase-12. Brain Res. *1519*, 1–8.

Gencic, S., Abuelo, D., Ambler, M., and Hudson, L.D. (1989). Pelizaeus-Merzbacher disease: an X-linked neurologic disorder of myelin metabolism with a novel mutation in the gene encoding proteolipid protein. Am. J. Hum. Genet. *45*, 435–442.

Gow, A., and Lazzarini, R.A. (1996). A cellular mechanism governing the severity of Pelizaeus-Merzbacher disease. Nat. Genet. *13*, 422–428.

Gow, A., Friedrich, V.L., Jr., and Lazzarini, R.A. (1994). Many naturally occurring mutations of myelin proteolipid protein impair its intracellular transport. J. Neurosci. Res. *37*, 574–583.

Gow, A., Gragerov, A., Gard, A., Colman, D.R., and Lazzarini, R.A. (1997). Conservation of topology, but not conformation, of the proteolipid proteins of the myelin sheath. J. Neurosci. *17*, 181–189.

Gow, A., Southwood, C.M., and Lazzarini, R.A. (1998). Disrupted proteolipid protein trafficking results in oligodendrocyte apoptosis

in an animal model of Pelizaeus-Merzbacher disease. J. Cell Biol. *140*, 925–934.

Griffiths, I., Klugmann, M., Anderson, T., Yool, D., Thomson, C., Schwab, M.H., Schneider, A., Zimmermann, F., McCulloch, M., Nadon, N., and Nave, K.A. (1998). Axonal swellings and degeneration in mice lacking the major proteolipid of myelin. Science *280*, 1610–1613.

Hodes, M.E., Aydanian, A., Dlouhy, S.R., Whelan, D.T., Heshka, T., and Ronen, G. (1998). A de novo mutation (C755T; Ser252Phe) in exon 6 of the proteolipid protein gene responsible for Pelizaeus-Merzbacher disease. Clin. Genet. *54*, 248–249.

Hu, B.Y., Du, Z.W., and Zhang, S.C. (2009). Differentiation of human oligodendrocytes from pluripotent stem cells. Nat. Protoc. *4*, 1614–1622.

Imaizumi, Y., Okada, Y., Akamatsu, W., Koike, M., Kuzumaki, N., Hayakawa, H., Nihira, T., Kobayashi, T., Ohyama, M., Sato, S., et al. (2012). Mitochondrial dysfunction associated with increased oxidative stress and α-synuclein accumulation in PARK2 iPSC-derived neurons and postmortem brain tissue. Mol. Brain *5*, 35.

Izrael, M., Zhang, P., Kaufman, R., Shinder, V., Ella, R., Amit, M., Itskovitz-Eldor, J., Chebath, J., and Revel, M. (2007). Human oligodendrocytes derived from embryonic stem cells: Effect of noggin on phenotypic differentiation in vitro and on myelination in vivo. Mol. Cell. Neurosci. *34*, 310–323.

Kang, S.M., Cho, M.S., Seo, H., Yoon, C.J., Oh, S.K., Choi, Y.M., and Kim, D.W. (2007). Efficient induction of oligodendrocytes from human embryonic stem cells. Stem Cells *25*, 419–424.

Lim, M.P., Devi, L.A., and Rozenfeld, R. (2011). Cannabidiol causes activated hepatic stellate cell death through a mechanism of endoplasmic reticulum stress-induced apoptosis. Cell Death Dis. *2*, e170.

Mikoshiba, K., Okano, H., Tamura, T., and Ikenaka, K. (1991). Structure and function of myelin protein genes. Annu. Rev. Neurosci. *14*, 201–217.

Nori, S., Okada, Y., Yasuda, A., Tsuji, O., Takahashi, Y., Kobayashi, Y., Fujiyoshi, K., Koike, M., Uchiyama, Y., Ikeda, E., et al. (2011). Grafted human-induced pluripotent stem-cell-derived neurospheres promote motor functional recovery after spinal cord injury in mice. Proc. Natl. Acad. Sci. USA *108*, 16825–16830.

Ohta, S., Imaizumi, Y., Okada, Y., Akamatsu, W., Kuwahara, R., Ohyama, M., Amagai, M., Matsuzaki, Y., Yamanaka, S., Okano, H., and Kawakami, Y. (2011). Generation of human melanocytes from induced pluripotent stem cells. PLoS ONE *6*, e16182.

Okada, Y., Shimazaki, T., Sobue, G., and Okano, H. (2004). Retinoic-acid-concentration-dependent acquisition of neural cell identity during in vitro differentiation of mouse embryonic stem cells. Dev. Biol. *275*, 124–142.

Okada, Y., Matsumoto, A., Shimazaki, T., Enoki, R., Koizumi, A., Ishii, S., Itoyama, Y., Sobue, G., and Okano, H. (2008). Spatiotemporal recapitulation of central nervous system development by murine embryonic stem cell-derived neural stem/progenitor cells. Stem Cells *26*, 3086–3098.

Seitelberger, F. (1995). Neuropathology and genetics of Pelizaeus-Merzbacher disease. Brain Pathol. *5*, 267–273.

Shimada, H., Okada, Y., Ibata, K., Ebise, H., Ota, S., Tomioka, I., Nomura, T., Maeda, T., Kohda, K., Yuzaki, M., et al. (2012). Efficient derivation of multipotent neural stem/progenitor cells from non-human primate embryonic stem cells. PLoS ONE *7*, e49469.

Shimojima, K., Inoue, T., Imai, Y., Arai, Y., Komoike, Y., Sugawara, M., Fujita, T., Ideguchi, H., Yasumoto, S., Kanno, H., et al. (2012). Reduced PLP1 expression in induced pluripotent stem cells derived from a Pelizaeus-Merzbacher disease patient with a partial PLP1 duplication. J. Hum. Genet. *57*, 580–586.

Southwood, C.M., Garbern, J., Jiang, W., and Gow, A. (2002). The unfolded protein response modulates disease severity in Pelizaeus-Merzbacher disease. Neuron *36*, 585–596.

Takahashi, K., Tanabe, K., Ohnuki, M., Narita, M., Ichisaka, T., Tomoda, K., and Yamanaka, S. (2007). Induction of pluripotent stem cells from adult human fibroblasts by defined factors. Cell *131*, 861–872.

Thomson, C.E., Montague, P., Jung, M., Nave, K.A., and Griffiths, I.R. (1997). Phenotypic severity of murine Plp mutants reflects in vivo and in vitro variations in transport of PLP isoproteins. Glia *20*, 322–332.

Wang, S., Bates, J., Li, X., Schanz, S., Chandler-Militello, D., Levine, C., Maherali, N., Studer, L., Hochedlinger, K., Windrem, M., and Goldman, S.A. (2013). Human iPSC-derived oligodendrocyte progenitor cells can myelinate and rescue a mouse model of congenital hypomyelination. Cell Stem Cell *12*, 252–264.

Yin, X., Baek, R.C., Kirschner, D.A., Peterson, A., Fujii, Y., Nave, K.A., Macklin, W.B., and Trapp, B.D. (2006). Evolution of a neuroprotective function of central nervous system myelin. J. Cell Biol. *172*, 469–478.

Experimental Neurology 261 (2014) 171–179

Contents lists available at ScienceDirect

Experimental Neurology

journal homepage: www.elsevier.com/locate/yexnr

Regular Article

Global gene expression analysis following spinal cord injury in non-human primates

Soraya Nishimura [a,b], Takashi Sasaki [c,d], Atsushi Shimizu [e], Kenji Yoshida [f], Hiroki Iwai [a,b], Ikuko Koya [b], Yoshiomi Kobayashi [a], Go Itakura [a,b], Shinsuke Shibata [b], Hayao Ebise [g], Keisuke Horiuchi [a], Jun Kudoh [h], Yoshiaki Toyama [a], Aileen J. Anderson [i], Hideyuki Okano [b,*], Masaya Nakamura [a,**]

[a] Department of Orthopedic Surgery, Keio University School of Medicine, 35 Shinanomachi, Shinjuku-ku, Tokyo 160-8582, Japan
[b] Department of Physiology, Keio University School of Medicine, 35 Shinanomachi, Shinjuku-ku, Tokyo 160-8582, Japan
[c] Department of Dermatology, Keio University School of Medicine, 35 Shinanomachi, Shinjuku-ku, Tokyo 160-8582, Japan
[d] Center for Integrated Medical Research, Keio University School of Medicine, 35 Shinanomachi, Shinjuku-ku, Tokyo 160-8582, Japan
[e] Division of Biomedical Information Analysis, Iwate Tohoku Medical Megabank Organization, Iwate Medical University, 2-1-1, Nishitokuta, Yahaba-cho, Shiwa-gun, Iwate 028-3694, Japan
[f] Regenerative & Cellular Medicine Office, Dainippon Sumitomo Pharma Co., Ltd., 3-1-98 Kasugade-naka, Konohana-ku, Osaka 554-0022, Japan
[g] Genomic Science Laboratories, Dainippon Sumitomo Pharma Co., Ltd., 3-1-98 Kasugade-naka, Konohana-ku, Osaka 554-0022, Japan
[h] Laboratory of Gene Medicine, Keio University School of Medicine, 35 Shinanomachi, Shinjuku-ku, Tokyo 160-8582, Japan
[i] Sue and Bill Gross Stem Cell Research Center, University of California, Irvine, CA, 92697, USA

ARTICLE INFO

Article history:
Received 2 December 2013
Revised 17 May 2014
Accepted 20 May 2014
Available online 27 May 2014

Keywords:
Spinal cord injury
Non-human primate
Microarray
mRNA sequencing

ABSTRACT

Spinal cord injury (SCI) is a devastating condition with no established treatment. To better understand the pathology and develop a treatment modality for SCI, an understanding of the physiological changes following SCI at the molecular level is essential. However, studies on SCI have primarily used rodent models, and few studies have examined SCI in non-human primates. In this study, we analyzed the temporal changes in gene expression patterns following SCI in common marmosets (*Callithrix jacchus*) using microarray analysis and mRNA deep sequencing. This analysis revealed that, although the sequence of events is comparable between primates and rodents, the inflammatory response following SCI is significantly prolonged and the onset of glial scar formation is temporally delayed in primates compared with rodents. These observations indicate that the optimal time window to treat SCI significantly differs among different species. This study provides the first extensive analysis of gene expression following SCI in non-human primates and will serve as a valuable resource in understanding the pathology of SCI.

Introduction

Spinal cord injury (SCI) results in a devastating loss of motor and sensory functions due to the poor regenerative capacity of the central nervous system. In the United States alone, approximately 12,000 patients are annually diagnosed with SCI. Despite recent advances in surgical techniques and our understanding of the biology of the spinal cord, few treatment options for SCI are available with marginal benefits for patients. A greater understanding of the pathology and the underlying molecular mechanisms of SCI is, therefore, imperative to develop a better therapeutic modality.

Contusion SCI initially causes the destruction of the blood–spinal cord barrier, and infiltration of inflammatory cells into the spinal cord ensues (Alexander and Popovich, 2009; Beck et al., 2010; Okano, 2002). Proinflammatory cytokines and reactive oxygen species (ROS) are generated by inflammatory cells and lead to secondary damage in the spinal cord (Bains and Hall, 2012; Kubota et al., 2012; Xiong et al., 2007). Thereafter, the acute inflammatory response subsides and is followed by the formation of a cystic cavity and a glial scar. Subsequently, the production of chondroitin sulfate proteoglycans (CSPGs) and extracellular matrix proteins with potent inhibitory activity against axonal growth (Ikegami et al., 2005; Silver and Miller, 2004) increases as the lesion develops into the chronic phase. In due course, changes in the spinal cord microenvironment become irreversible (Afshari et al., 2009; Okano, 2002). We and others have extensively analyzed the temporal

Abbreviations: SCI, spinal cord injury; ROS, reactive oxygen species; CSPGs, chondroitin sulfate proteoglycans; mRNA-seq, mRNA sequencing; WPI, week-post-injury; PCA, principal component analysis; GO, gene ontology; HE, hematoxylin–eosin; PECAM-1, platelet endothelial cell adhesion molecule-1; PC, principal component; VEGF, vascular endothelial growth factor; MMP9, matrix metalloproteinase 9.

* Corresponding author. Fax: +81 3 3357 5445.
** Corresponding author. Fax: +81 3 3353 6597.
E-mail addresses: soraya-n@z8.keio.jp (S. Nishimura), sasasa@z5.keio.jp (T. Sasaki), chromosome8q23@gmail.com (A. Shimizu), kenji-yoshida@ds-pharma.co.jp (K. Yoshida), iwai@a7.keio.jp (H. Iwai), koya-ikuko@a5.keio.jp (I. Koya), y.kobayashi@z7.keio.jp (Y. Kobayashi), itakura@a2.keio.jp (G. Itakura), shibata@2001.jukuin.keio.ac.jp (S. Shibata), hayao-ebise@ds-pharma.co.jp (H. Ebise), horiuchi@z3.keio.jp (K. Horiuchi), jkudoh@dmb.med.keio.ac.jp (J. Kudoh), toyama@z6.keio.jp (Y. Toyama), aja@uci.edu (A.J. Anderson), hidokano@a2.keio.jp (H. Okano), masa@a8.keio.jp (M. Nakamura).

http://dx.doi.org/10.1016/j.expneurol.2014.05.021
0014-4886/

changes in gene expression patterns following SCI using rodent models (Beck et al., 2010; Kumamaru et al., 2012; Nakamura et al., 2003). These results not only provide important information to understand the molecular pathology of SCI but also serve as the basis to determine the optimal time window for therapeutic interventions, such as neural stem/progenitor cell transplantation (Abematsu et al., 2010; Cao et al., 2001; Cummings et al., 2005; Nishimura et al., 2013; Nori et al., 2011; Ogawa et al., 2002; Okada et al., 2005; Okano et al., 2013; Tsuji et al., 2010) and administration of anti-inflammatory substances and growth factors (Kitamura et al., 2011; Mukaino et al., 2010; Okada et al., 2004; Tuszynski et al., 1996). As highlighted by the studies in rodent models, it is conceivable that similar analyses in primate models will further deepen our understanding of the pathology of SCI in humans; however, such a study has not yet been performed, and very little is currently known regarding the changes in gene expression following SCI in primates.

To address this issue, we used the common marmoset (*Callithrix jacchus*) as a non-human primate SCI model and performed two different global gene expression analyses: microarray analysis and mRNA sequencing (mRNA-seq) using next-generation sequencing. Additionally, we performed a detailed histological analysis of the injured spinal cord in adult common marmosets to validate the gene expression analysis data. We found that, although the sequence of the gene expression patterns was comparable between common marmosets and rodents, the time course of changes in gene expression was significantly prolonged in common marmosets. This observation indicates that the transition of SCI from the acute to the chronic phase is temporally delayed in common marmosets compared with rodents and that the therapeutic time window following SCI significantly differs among species. This study provides the first extensive gene expression analysis following SCI in non-human primates and may serve as an invaluable resource in understanding the pathology following SCI in primates and in establishing a time frame for the treatment of SCI in humans.

Materials and methods

Animals

All interventions and animal care procedures were performed in accordance with the Laboratory Animal Welfare Act, the Guide for the Care and Use of Laboratory Animals (National Institutes of Health, USA), the Guidelines and Policies for Animal Surgery provided by the Animal Study Committee of the Central Institute for Experimental Animals and Keio University, and the guidelines outlined by the Weatherall Report and were approved by the Animal Study Committee of Keio University (numbers: 10017 and 11014). Female common marmosets (*C. jacchus*; 2-years-old) were purchased from CLEA Japan Inc. (Tokyo, Japan). The animals were housed at 26 °C with 65% humidity and illumination for 12 h/day. All of the animals had free access to food and water in the cage.

Contusive SCI in common marmosets

The subjects were anesthetized with an intramuscular injection of ketamine (50 mg/kg; Sankyo Co., Ltd., Tokyo, Japan) and xylazine (5 mg/kg; Bayer AG, Leverkusen, Germany), followed by inhalation of isoflurane (Fluren; Abbott Japan Co., Ltd., Tokyo, Japan). Contusive SCI was induced using a modified New York University weight-drop device, as previously described (Iwanami et al., 2005; Kobayashi et al., 2012). Briefly, a 17-g weight, 3.5 mm in diameter, was dropped from a height of 50 mm onto the exposed dura mater at the C5 level following laminectomy. For the sham control, laminectomy of the C5 vertebra was performed without any manipulation of the spinal cord. During the surgical procedures, the physiological condition of the animals was continuously monitored by electrocardiography, transcutaneous pulse oximetry (which estimates O_2 saturation), and skin and rectal temperature readings. After the procedure, the animals were placed in a temperature-controlled chamber until thermoregulation was reestablished. Manual bladder expression was performed twice per day until voiding reflexes were reestablished. Paralyzed animals were provided adequate amounts of food and water until they recovered their ability to ingest food and water without assistance. Thereafter, animals had free access to food and water in the cage.

RNA isolation

The animals were anesthetized and transcardially perfused with heparinized saline (5 U/ml) at 1-, 2-, 4-, and 6-weeks-post-injury (WPI). Dissected segments (6 mm) of the spinal cord at the C5 level were placed in TRIzol (Invitrogen, Carlsbad, CA, USA) and immediately frozen. Total RNA was isolated using a Qiagen RNeasy Kit (Qiagen Inc., Hilden, Germany). Samples were collected from two different animals with SCI at each time point following injury and one sham control animal at 2-WPI.

Microarray analysis

Microarray analysis was performed using Affymetrix GeneChip technology as previously described (Heishi et al., 2006; Matsui et al., 2012). Sham control samples were independently analyzed three times. Total RNA (100 ng) was reverse transcribed, biotin labeled, and hybridized for 16 h to the Marmoset Genome oligonucleotide custom array Marmo2 (Shimada et al., 2012; Tomioka et al., 2010). The arrays were subsequently washed and stained in a Fluidics Station 450 (Affymetrix Japan, Tokyo, Japan) according to the manufacturer's instructions. The arrays were scanned using a GeneChip Scanner 3000 7G (Affymetrix Japan). Data analysis was performed using Expression Console 1.1 (Affymetrix Japan). Signal detection and quantification were performed using the MAS5 algorithm with the default settings. Principal component analysis (PCA) was performed using Spotfire DecisionSite 9.1.2 (TIBCO Spotfire, Somerville, MA, USA). Statistical analysis was performed using one-way ANOVA followed by the Tukey–Kramer test ($P < 0.001$) using GeneSpring GX software 11.5.1 (Agilent Technologies Inc., Santa Clara, CA, USA). The heat map was visualized using Java TreeView (Saldanha, 2004). A total of 708 genes were grouped into eight clusters by K-means clustering using Gene Spring GX software 11.5.1 (Agilent Technologies Inc.). Gene ontology (GO) analysis was performed using the gene lists of each cluster. Enriched GO terms were extracted using corrected *P* values with a cut-off at 0.05. *P* values were calculated using Fisher's exact test. To obtain the corrected *P* values, the false discovery rate was controlled using the Benjamini–Yekutieli method.

Library preparation and mRNA-seq

Samples for mRNA-seq were prepared using the TruSeq RNA Sample Prep Kit (Illumina, San Diego, CA, USA) according to the manufacturer's protocol. Briefly, 100 ng of each total RNA sample was used for poly-A mRNA selection using poly-T oligonucleotides attached to magnetic beads. The purified mRNA was then fragmented and subjected to cDNA synthesis using random primers. Following conversion of the fragmented mRNA to double-stranded cDNA, a single adenosine nucleotide was added to the 3′ ends of the blunted cDNA fragments and then ligated to the Y-shape adapter. These cDNAs were purified using AMPure beads (Beckman Coulter, Brea, CA, USA) to remove excess adapter. Finally, the cDNA libraries were amplified by PCR and purified using AMPure beads. Each library was adjusted to a concentration of 11–12 pM and analyzed using a Genome Analyzer IIx (Illumina) in 75-bp single-read mode. The marmoset genomic DNA sequence including scaffold sequences was obtained from the Ensembl FTP site (ftp://ftp.ensembl.org/); concatemerized scaffold sequences were treated as single chromosomes and indexed using bowtie-build v.0.12.7

(Langmead et al., 2009). The marmoset mRNA-seq reads were mapped to the concatemerized marmoset genomic DNA sequence using TopHat v.1.3.1 (http://tophat.cbcb.umd.edu/) (Trapnell et al., 2009) with the following parameters: "num-threads", 4, and "splice-mismatches", 2. The BAM-formatted mapping sequence data were normalized using the trimmed mean of M values method, and the expression of each gene was analyzed using Avadis NGS software (Agilent Technologies Inc.).

Histological analysis

The subjects were anesthetized and intracardially perfused with 4% paraformaldehyde at 1-, 2-, and 6-WPI (n = 2 each). A segment (6 mm) of the spinal cord including the lesion epicenter was removed at the C5 level, fixed overnight in 4% paraformaldehyde, and consecutively soaked overnight in 10% and 30% sucrose. Each sample was embedded in Optimal Cutting Temperature compound (Sakura Finetechnical Co., Ltd., Tokyo, Japan), frozen, and sectioned in the sagittal plane on a cryostat into 20-μm-thick sections. The sections were stained with hematoxylin–eosin (HE) for general histological examination or immunostained with the following primary antibodies: anti-Iba1 (rabbit IgG, 1:200, Wako Pure Chemical Industries, Osaka, Japan), anti-GFAP (rat IgG, 1:200, Invitrogen, Carlsbad, CA, USA), anti-CS56 (which is a marker of CSPGs, mouse IgM, 1:200, Sigma-Aldrich, St. Louis, MO, USA), anti-ephrin B3 (rabbit IgG, 1:200, Abcam, Cambridge, UK), anti-platelet endothelial cell adhesion molecule-1 (PECAM-1) (rat IgG, 1:50, BD Biosciences-Pharmingen, San Diego, CA, USA), anti-CD11b (rat IgG, 1:200, BD Biosciences-Pharmingen), and anti-Ki67 (rabbit IgG, 1:200, Leica Biosystems). For immunohistochemistry using anti-GFAP and anti-PECAM-1 antibodies, a biotinylated secondary antibody (Jackson ImmunoResearch Laboratories, Inc., West Grove, PA, USA) was used after exposing the sections to 0.3% H_2O_2 for 30 min at room temperature to inactivate endogenous peroxidases. The signals were enhanced using the VECTASTAIN ABC kit (Vector Laboratories, Inc., Burlingame, CA, USA). Nuclei were stained with Hoechst 33258 (10 μg/ml, Sigma-Aldrich). All images were obtained using a fluorescence microscope (BZ-9000; Keyence Co., Osaka, Japan) or a confocal laser scanning microscope (LSM 700; Carl Zeiss, Munich, Germany).

Results

Global gene expression analysis using microarray analysis and mRNA-seq

Currently, the genome database for the common marmoset remains incomplete and numerous scaffolds exist in the gene model; consequently, there is a risk of inadequately over- or underestimating the expression levels of certain genes that are located across the scaffold and known chromosomes. Therefore, we applied both microarray analysis and mRNA-seq to examine gene expression profiles in this study. We performed contusive SCI on 2-year-old common marmosets as previously described (Iwanami et al., 2005; Kobayashi et al., 2012) and collected the spinal tissues at 1-, 2-, 4-, and 6-WPI. For microarray analysis, gene expression data using the Marmo2 array were normalized by setting the average of the signal value of all of the probe sets to 100. Probe sets without a significant signal were excluded from the subsequent analysis. A total of 17,653 genes were identified in each specimen using microarray analysis. In mRNA-seq analysis, sequence tag counts were used to directly determine transcript abundance using homologous fractions from the present marmoset gene models. From the 21,716 sequences analyzed using mRNA-seq, 16,863 genes were uniquely matched with the microarray data using the Ensembl database. Regression analyses of the quantified expression values at each time point between the mRNA-seq and microarray data exhibited R^2 values comparable to previous studies using different animal models (Fig. 1, R^2 = 0.570-0.607) (Llorens et al., 2011; Mortazavi et al., 2008; Wang et al., 2009). These results indicate that, although these methods can be further optimized, both methods demonstrate applicability for gene expression analysis in this study.

Overview of the gene expression patterns in the spinal cord following injury

To gain an overview of the temporal changes in the transcriptome following SCI, we performed PCA with three principal components (PC1, 2, and 3) using the microarray data. The contribution of each component was 30.7%, 21.6%, and 13.0%, respectively. Three-dimensional PC score plots indicated that the two individual specimens harvested at identical time points following SCI were closely clustered together, validating the reproducibility of the present analysis (Fig. 2A). The localization of the plots from the 1-WPI samples was significantly different from that of the sham control on the PC1 axis, indicating that the difference on the PC1 axis most likely represents the presence or absence of injury. Notably, the 2- and 4-WPI group clusters, which were located close to one another, exhibited a largely different localization from that of the 1-WPI cluster, particularly on the PC2 axis, indicating that the gene expression pattern significantly changes 1 week following injury to the spinal cord. Although the localization of the 6-WPI group cluster was slightly different from the localizations of the 2- and 4-WPI clusters on the PC3 axis, these plots were nevertheless nearly identically distributed on the three-dimensional plane.

To extract the principal genes involved in the development of post-SCI changes, the normalized data were reduced to 708 genes using the cut-off values of the expression levels (>50) and the fold change (>3.0) versus the signal value of the sham-operated control. Two-dimensional hierarchical clustering indicated that the sham group and the SCI groups each formed a distinct cluster (Fig. 2B). Although the gene expression patterns within each SCI group were similar, the degree of changes in the gene expression patterns from that of the sham group was significantly higher in the 1-WPI group than in the other SCI groups (2-, 4-, and 6-WPI). Consistent with the PCA, the tree view exhibited a relatively high correlation between the 2- and 4-WPI groups, whereas no significant correlation between the 2-, 4-, and 6-WPI groups and the 1-WPI group was observed. Collectively, these results suggest that the changes in the gene expression patterns following SCI can be approximately divided into two phases: the acute phase (0–2 weeks following injury, during which period the gene expression patterns drastically fluctuate) and the subacute/chronic phase (2–6 weeks following injury, during which period the gene expression patterns gradually converge to a steady state).

K-means clustering and GO analysis of target genes

We next performed K-means clustering and GO analysis to further investigate the biological characteristics of the extracted genes. Because our original marmoset GeneChip sets were not annotated with GO terms, each probe was linked with the corresponding GO terms of human genes via the human RefSeq database. Using K-means clustering, the target genes were statistically grouped into eight clusters according to their expression patterns following SCI. GO analysis was individually performed on each cluster, and GO terms of interest were obtained from five of the eight clusters (Fig. 3). Based on the time course of the gene expression pattern changes, we found that these five clusters can be divided into three different groups. Cluster 1 represents the genes that are downregulated following SCI. The GO terms in this cluster are primarily related to synaptic transmission and neurotransmitters, which reflect the loss of functional neural tissues following SCI. Clusters 2 and 3 represent the genes that are upregulated following SCI. The GO terms in these two clusters are related to the immune response and the production of cytokines, which are indicative of the inflammatory reaction evoked following SCI. The gene expression patterns in these two groups (Clusters 1, 2, and 3) indicate that the genes in these clusters are responsible for the drastic changes in the gene expression patterns following SCI, as shown in the three-

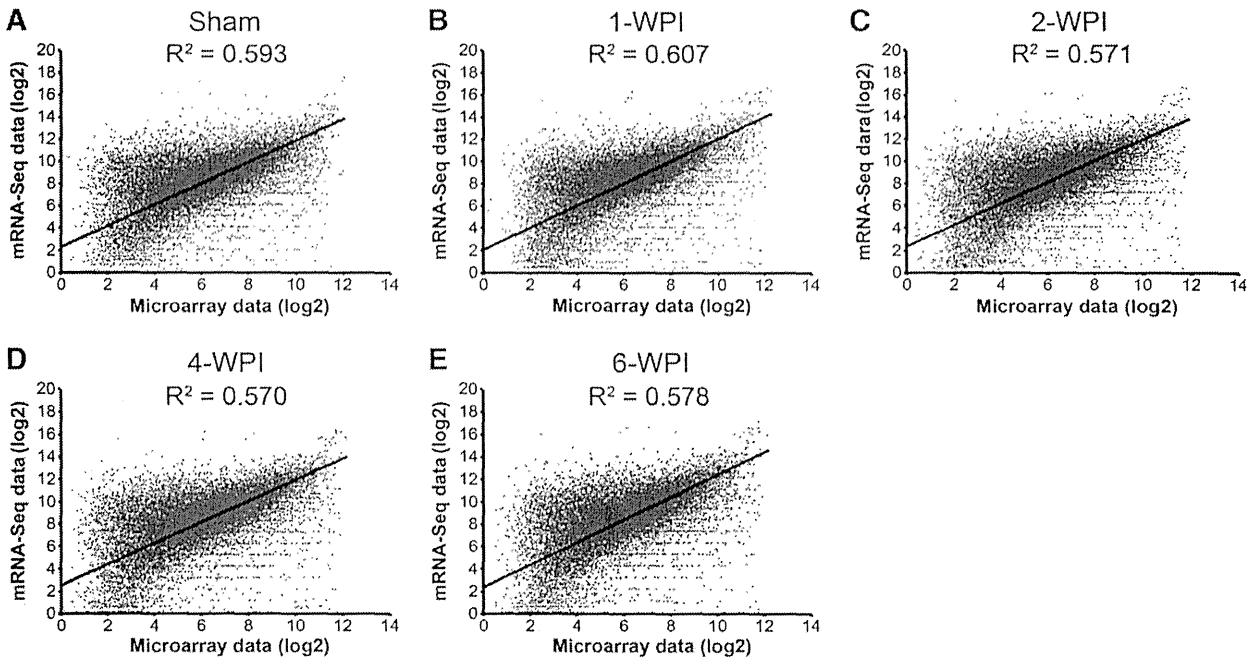

Fig. 1. Comparison of the gene expression patterns in the injured spinal cord between the microarray and mRNA-seq analyses. The spinal cord tissues were collected from the sham-operated marmoset (A) and the marmosets with SCI at 1- (B), 2- (C), 4- (D), and 6-WPI (E), and the gene expression levels were analyzed using microarray analysis and mRNA-seq as described in the Materials and methods.

dimensional PC score plots and hierarchical clustering (Figs. 2A and B). In contrast, Clusters 4 and 5 represent the genes that are transiently up-regulated following SCI and subsequently repressed to near basal levels. The GO terms in this cluster are primarily related to the regulation of ROS and the cell cycle, reflecting the genes involved in the regulation of post-traumatic oxidative damage and robust cell proliferation. Because the expression levels of the genes in this group (Clusters 4 and 5) peak at 1-WPI and decrease thereafter, these genes likely represent the determinants in discriminating the gene expression profiles of the 1-WPI group from those of other SCI groups in PCA and hierarchical clustering (Figs. 2A and B).

The development of the secondary changes following SCI is delayed in common marmosets compared with rodents

Previous studies suggest that the optimum therapeutic time window for SCI differs for each individual therapeutic intervention. For example, cell transplantation is most effective when it is performed during the transition period from the inflammatory phase to the onset of glial formation. In contrast, the administration of anti-inflammatory substances and growth factors should be performed before the inflammatory response subsides. In rodent models, the production of inflammatory cytokines sharply increases as early as 12 h following injury and

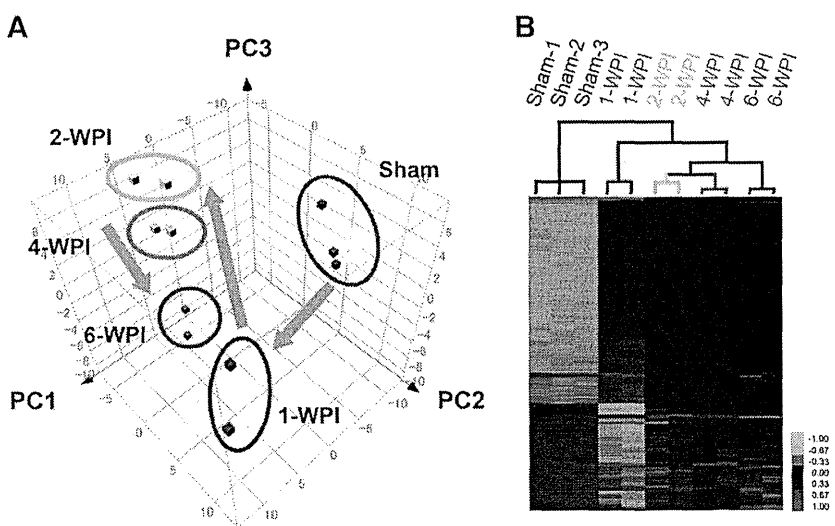

Fig. 2. Temporal changes in the gene expression pattern following SCI. (A) Three-dimensional PC score plots of the microarray data. (B) Hierarchical clustering of the principal genes. Blue tiles indicate downregulated genes, and magenta tiles indicate upregulated genes.

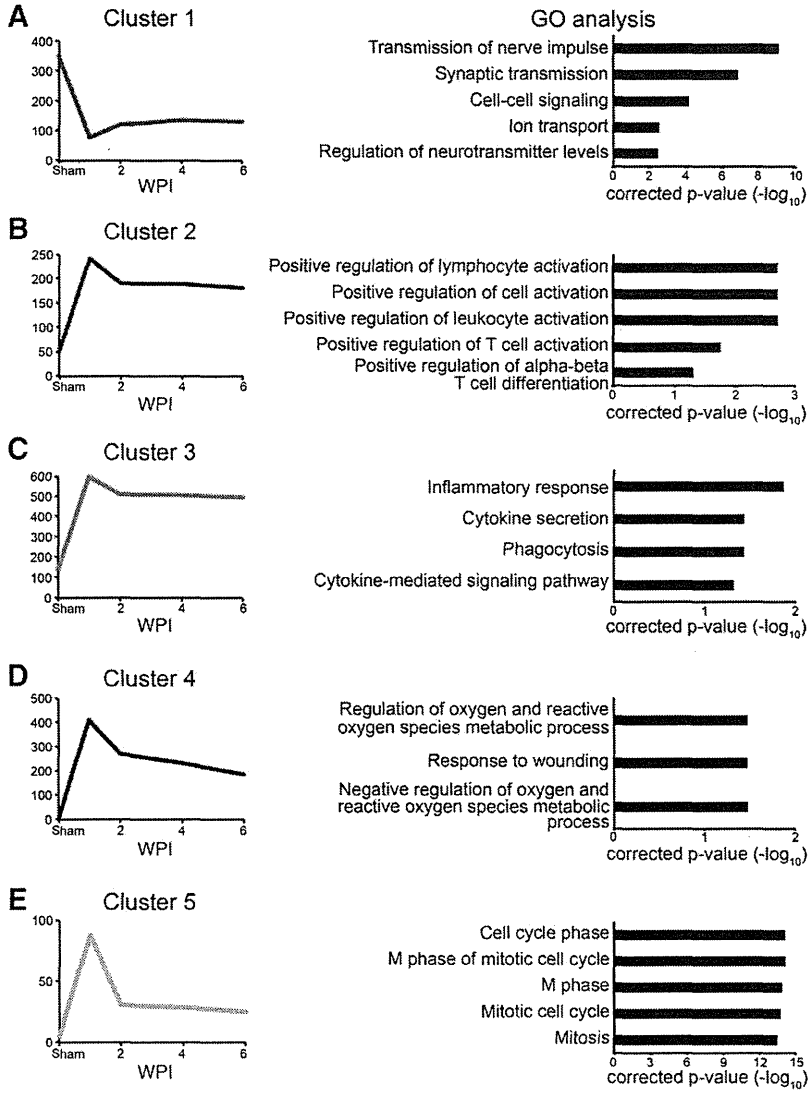

Fig. 3. GO analysis of the genes involved in the development of post-SCI changes. (A–E) Genes involved in the development of post-SCI changes were grouped into five clusters using K-means analysis, and the GO terms were annotated in each cluster.

diminishes to near basal levels by 1-WPI (Kumamaru et al., 2012; Nakamura et al., 2003). In contrast, the present GO analysis suggests that the inflammatory response is significantly prolonged in primates compared with rodents, indicating that the therapeutic time window differs among species. To validate this hypothesis, we further analyzed the genes involved in the inflammatory response and found that the expression levels of immune cell markers and cytokines peak at 1-WPI and decrease at and after 2-WPI (Figs. 4A and B). This trend was nearly identical between the results of the microarray and mRNA-seq analyses. Moreover, these observations are consistent with the results of GO analyses, suggesting that the inflammatory response following SCI is prolonged in primates compared with rodents.

Based on the observation that the overall inflammatory phase following SCI is extended in primates, we next asked whether the onset of the chronic phase (i.e., the expression of axonal growth inhibitors and glial scar formation) also follows this trend. We found that the expression of ephrin B3, which is a well-known axonal growth inhibitor (Duffy et al., 2012), increases at and after 1–2-WPI (Fig. 4D). The changes in the expression level of CSPGs, which are a family of proteins that exhibit potent inhibitory activity against axonal growth, were less evident; however, phosphacan exhibited a significant increase at 2-WPI in mRNA-seq analysis (Fig. 4E). Additionally, a temporal increase in vascular endothelial growth factor (VEGF) B transcripts at 2-WPI was observed (Fig. 4C). As expected, myelin-associated proteins, such as myelin basic protein and proteolipid protein 1, significantly decreased following SCI and slightly recovered thereafter in mRNA-seq analysis (Fig. 4F). These results suggest that the endogenous repair responses including revascularization and remyelination occur at approximately 2-WPI in the present model. Although there were some discrepancies between the results of microarray and mRNA-seq analyses, these trends were nearly identical between the two analyses. Collectively, these observations suggest that the transition period from the inflammation phase to the onset of glial scar formation lies at approximately 2-WPI in primates and is significantly delayed in common marmosets compared with rodents.

Histological analysis of the injured spinal cord in common marmosets

To further validate the results of the transcriptome analysis at the protein level, we performed histological analysis of the injured spinal cord in common marmosets. Immunostaining indicated a marked infiltration of $Iba1^{+}$ macrophages and microglial cells at the lesion epicenter

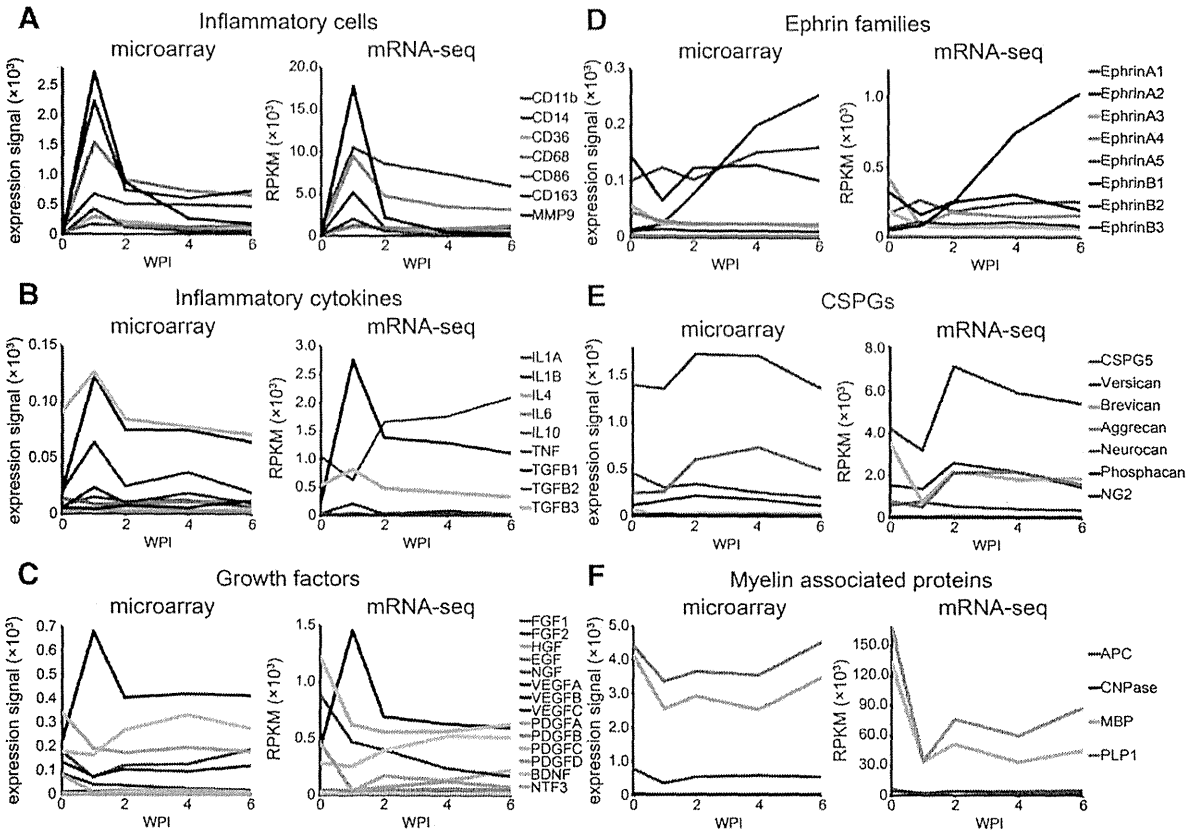

Fig. 4. Comparison of the temporal changes in gene expression between mRNA-seq and microarray analyses. The expression of a portion of the major genes involved in the early stage (A–C) and later stage (D–F) of the development of post-SCI changes were quantitatively analyzed.

at 1-WPI (Fig. 5B-1), whereas no positive staining for GFAP or CS56 was observed at this time point (Fig. 5C-1). Ephrin B3 was present at only low levels in the lesion at 1-WPI (Fig. 5E-1). Additionally, we found $CD11b^{+}$ $Ki67^{+}$ cells at the lesion epicenter at 1-WPI, indicating that the infiltrated macrophages and microglial cells were actively proliferating in situ at this time point (Fig. 5G). None of these cells were detected at and after 2-WPI. These observations are consistent with the GO analysis, in which several GO terms associated with cell proliferation (Fig. 3, Cluster 5) were identified at 1-WPI (Fig. 3E). The number of $Iba1^{+}$ cells significantly decreased at 2-WPI, and conversely,

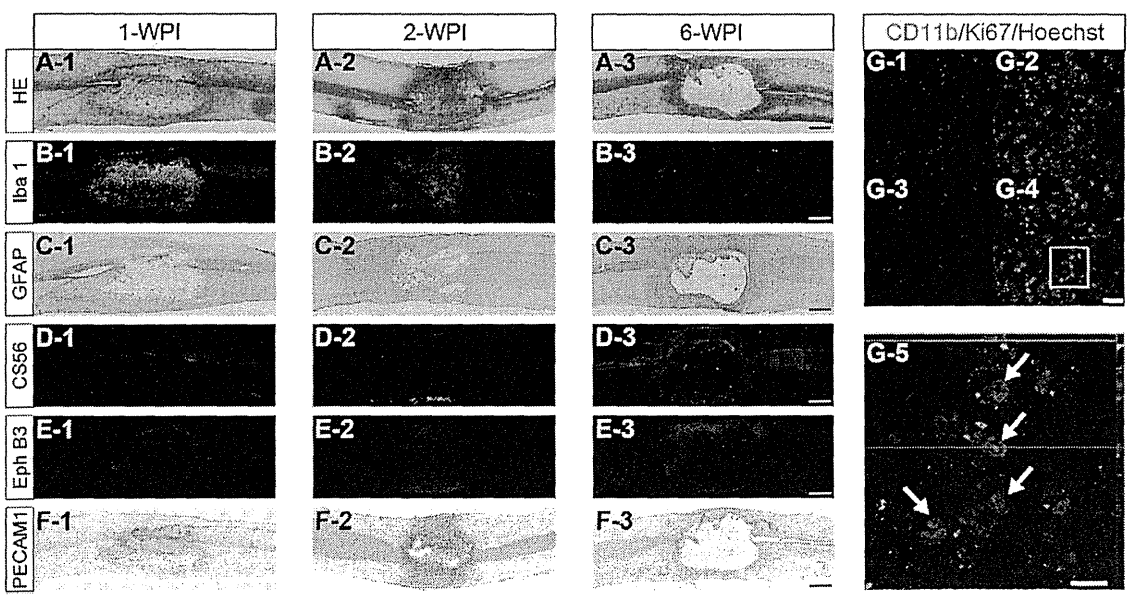

Fig. 5. Histological analysis of the temporal changes in the injured spinal cord tissues. Representative images of sagittal sections of spinal cord tissues collected at 1-, 2-, and 6-WPI. HE staining (A) and immunostaining for Iba1 (B), GFAP (C), CS56 (D), ephrin B3 (E), and PECAM-1 (F). Arrows (G-5) indicate the cells dually positive for CD11b and Ki67. Scale bars: 500 μm in (A, B, C, D, E, and F), 50 μm in (G-1–4), and 10 μm in (G-5).

an increase in the positive staining for PECAM-1 (which is an endothelial cell marker) at the lesion site was observed (Fig. 5B-2). At this time point, the ephrin B3-positive areas became evident, whereas the GFAP- and CS56-positive areas remained undetectable. By 6-WPI, Iba1$^+$ cells had all disappeared from the lesion (Fig. 5B-3), and the formation of a cavity at the epicenter became evident. The cavity was delineated by a GFAP-positive glial scar that was positive for CS56 and ephrin B3 (Figs. 5A-3, C-3, D-3, and E-3). The PECAM-1-positive vascular area, which was present at 2-WPI, could no longer be detected around the cavity at this time point (Fig. 5F-3). Overall, these temporal changes in the histological analysis are consistent with the analytical data deduced from the gene expression analyses and support the validity of the present transcriptome analysis methodology.

Discussion

To understand the pathology of SCI and to establish a better treatment, global analysis of the gene expression patterns of the injured spinal cord is critical. Previous studies primarily utilized rodent SCI models for this purpose (Beck et al., 2010; Kumamaru et al., 2012; Nakamura et al., 2003), and, to the best of our knowledge, no primate models have been previously employed. Thus, the question remained whether the transcriptome results from rodent models is applicable to primates. In this study, we performed extensive gene expression and histological analyses in an adult common marmoset SCI model and present the first results on the temporal changes in gene expression patterns following SCI in primates.

This study reveals important differences and similarities in the temporal changes in gene expression patterns of the injured spinal cord between primates and rodents. For example, a significant accumulation of macrophages and microglial cells in the injured spinal cord was observed at approximately 1-WPI in both primates (the present study, Figs. 4A and 5B) and rodents (Beck et al., 2010; Popovich et al., 1997). The temporal changes in the production of ROS, which play a crucial role in post-traumatic oxidative damage (Bains and Hall, 2012; Kubota et al., 2012; Xiong et al., 2007), also appeared to be similar between primates and rodents. In contrast, previous studies using a rodent SCI model indicated that the increase in the production of inflammatory cytokines returns to near basal levels by 1-WPI (Kumamaru et al., 2012; Nakamura et al., 2003), whereas in common marmosets, the expression of proinflammatory cytokines remained at relatively high levels at 1-WPI and decreased to basal levels at approximately 2-WPI (Fig. 4B). Additionally, we found that the expression of matrix metalloproteinase 9 (MMP9) transcripts, which peaks within 24 h following injury in rodent SCI models (Lee et al., 2012b; Noble et al., 2002), was expressed at significantly elevated levels at 1-WPI in primates (Fig. 4A). MMP9 is expressed in activated macrophages/microglial cells (Lee et al., 2012a; Lee et al., 2012b); therefore, this observation supports the idea that the inflammatory response following SCI requires a longer time to subside in primates than in rodents. Collectively, these observations suggest that, although the sequence of events following SCI is comparable between primates and rodents, the inflammatory response following SCI is significantly longer in primates than in rodents.

Some discrepancies were found between the transcriptome and histological analyses with regard to certain genes. Temporal expression patterns of ephrin B3 were similar between the transcriptome and histological analyses, which indicated a gradual increase after 1-WPI in both analyses. Additionally, the increase in the *VEGFB* transcripts and the formation of the vasculature (PECAM-1-positive areas), as well as the expression of immune cell markers and the appearance of Iba1$^+$ cells, were both nearly synchronized. In contrast, although the accumulation of CSPGs (CS56-positive areas) in the injured spinal cord became evident at 6-WPI, the expression of the CSPG transcripts remained rather constant throughout the time course following SCI. Although the reason for this discrepancy is unclear, newly produced CSPGs may be consistently accumulated in the site of injury without being degraded following SCI.

Several therapeutic approaches, such as cell transplantation and growth factor administration, have been shown to induce functional recovery following SCI in several animal models. In the acute phase of SCI, inflammatory cytokines exhibit neurotoxic effects on neural progenitor cells (Andrews et al., 1998; Ben-Hur et al., 2003) and drive cellular differentiation toward the astrocyte lineage (Gomi et al., 2011; Okada et al., 2005). However, in the chronic phase, glial scar formation prevents the migration of neural progenitor cells and axonal growth (Afshari et al., 2009; Ikegami et al., 2005; Kumamaru et al., 2013; Nishimura et al., 2013; Silver and Miller, 2004). These studies suggest that the optimal time window of cell transplantation therapy lies between the cessation of the inflammatory response and the onset of glial scar formation, which is approximately 7–9 days following SCI in rodents (Abematsu et al., 2010; Cao et al., 2001; Cummings et al., 2005; Lu et al., 2012; Nishimura et al., 2013; Ogawa et al., 2002; Okada et al., 2005; Tsuji et al., 2010). In contrast, neuroprotective approaches, such as the administration of anti-inflammatory substances and growth factors, should be performed during the acute inflammatory phase, which resolves within 1-WPI in rodents. However, this study demonstrates that the acute inflammatory response following SCI, including the infiltration of inflammatory cells, inflammatory cytokine secretion, and oxidative damage, may continue until 2-WPI in common marmosets. Accordingly, the expression of axonal growth inhibitors gradually increased at approximately 2-WPI and thereafter. Furthermore, the accumulation of CSPGs and ephrin B3, as well as glial scar formation, were more prominent at 6-WPI than at 1- or 2-WPI, suggesting that the microenvironment of the injured spinal cord changes into an irreversible chronic stage by 6-WPI. Collectively, these results suggest that the optimal time window for cell transplantation may lie at approximately 2–4-WPI in non-human primates and 0–2-WPI for neuroprotective therapies (Fig. 6).

Due to the paucity of clinical data, it is unclear whether this time window is also applicable to humans; however, a previous study has demonstrated that the infiltrated inflammatory cells maintained their neurotoxic activity up to approximately 10 days following SCI in humans (Fleming et al., 2006). If this finding holds true, it is possible that humans also develop post-SCI changes in a similar time frame as common marmosets. Regarding the clinical application of cell transplantation for patients with SCI, the determination of the time window for efficient treatment and for the preparation of the cells for implantation is critical. Additional studies are warranted to better understand the temporal changes in gene expression and to determine the optimum time window for the treatment of SCI in humans. Nevertheless, we believe that the present study will serve as a foundation to accomplish these goals.

Author contributions

S.N., H.I., Y.K., H.O., and M.N. designed the research; S.N., K.Y., H.I., Y.K., and G.I. performed the research; S.N., T.S., A.S., K.Y., I.K., S.S., and H.E. analyzed the data; S.N., T.S., K.Y., K.H., A.A., H.O., and M.N. wrote the paper; and J.K., Y.T., H.O., and M.N. supervised all of the experiments.

Competing interests

H. Okano is a scientific consultant at San Bio Inc., Eisai Co. Ltd. and Daiichi Sankyo Co. Ltd. The remaining authors declare no conflicts of interest.

Acknowledgments

We thank Drs. A. Iwanami, K. Fujiyoshi, O. Tsuji, Y. Takahashi, M. Shinozaki, A. Yasuda, S. Nori, T. Konomi, M. Takano, R. Zhang, S. Tashiro, S. Kawabata, Y. Nishiyama, K. Hori, M. Ozaki, T. Iida, and K.

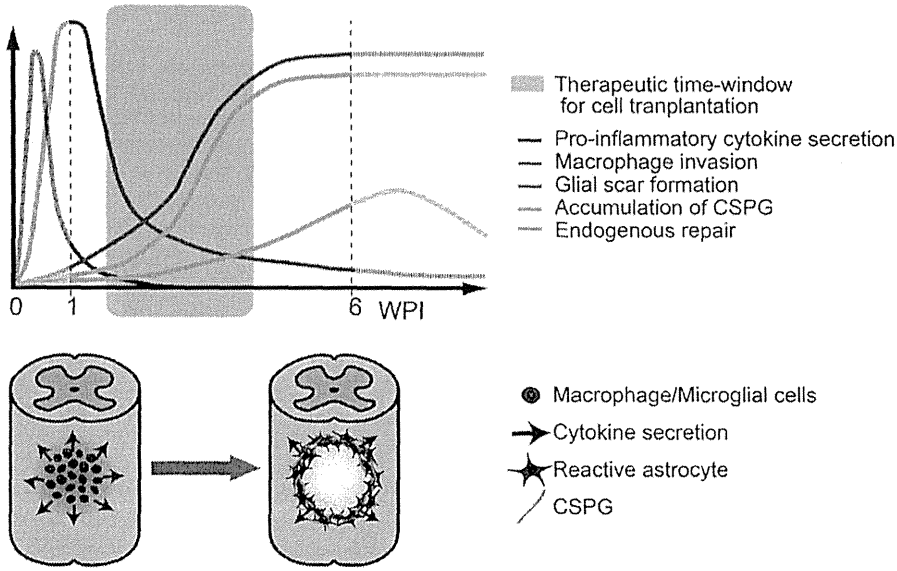

Fig. 6. Proposed schema of the post-SCI changes in primates. The initial inflammatory response following SCI resolves by 2-WPI. However, the expression of axonal growth inhibitors, as well as the accumulation of CSPGs and glial scar formation, gradually increases at 2-WPI and thereafter. These results suggest that the optimal time window for cell transplantation (i.e., the subacute phase of SCI) most likely lies at approximately 2–4-WPI in non-human primates.

Matsubayashi, who are the members of the spinal cord research team in the Departments of Orthopedic Surgery, Rehabilitation Medicine, and Physiology, at Keio University School of Medicine for their assistance. We thank Dr. H. Nakagawa for support with the data analysis. We thank Dr. Y. Sakakibara for providing the marmoset genome material. We also thank Mses. N. Hashimoto, T. Ishibuchi, S. Miyao, and M. Mizutani for their assistance with the experiments and animal care.

This work was supported by grants from the Japan Science and Technology–California Institute for Regenerative Medicine collaborative program; Grants-in-Aid for Scientific Research from the Japan Society for the Promotion of Science (SPS) and the Ministry of Education, Culture, Sports, Science, and Technology of Japan (MEXT); the Project for Realization of Regenerative Medicine; Support for Core Institutes for iPS Cell Research from the MEXT; Keio Gijuku Academic Development Funds; Funding Program for World-leading Innovative R&D on Science and Technology; and by a Grant-in-Aid for Scientific Research on Innovative Areas (Comprehensive Brain Science Network) from the MEXT.

References

Abematsu, M., Tsujimura, K., Yamano, M., Saito, M., Kohno, K., Kohyama, J., Namihira, M., Komiya, S., Nakashima, K., 2010. Neurons derived from transplanted neural stem cells restore disrupted neuronal circuitry in a mouse model of spinal cord injury. J. Clin. Invest. 120, 3255–3266.

Afshari, F.T., Kappagantula, S., Fawcett, J.W., 2009. Extrinsic and intrinsic factors controlling axonal regeneration after spinal cord injury. Expert Rev. Mol. Med. 11, e37.

Alexander, J.K., Popovich, P.G., 2009. Neuroinflammation in spinal cord injury: therapeutic targets for neuroprotection and regeneration. Prog. Brain Res. 175, 125–137.

Andrews, T., Zhang, P., Bhat, N.R., 1998. TNFalpha potentiates IFNgamma-induced cell death in oligodendrocyte progenitors. J. Neurosci. Res. 54, 574–583.

Bains, M., Hall, E.D., 2012. Antioxidant therapies in traumatic brain and spinal cord injury. Biochim. Biophys. Acta 1822, 675–684.

Beck, K.D., Nguyen, H.X., Galvan, M.D., Salazar, D.L., Woodruff, T.M., Anderson, A.J., 2010. Quantitative analysis of cellular inflammation after traumatic spinal cord injury: evidence for a multiphasic inflammatory response in the acute to chronic environment. Brain 133, 433–447.

Ben-Hur, T., Ben-Menachem, O., Furer, V., Einstein, O., Mizrachi-Kol, R., Grigoriadis, N., 2003. Effects of proinflammatory cytokines on the growth, fate, and motility of multipotential neural precursor cells. Mol. Cell. Neurosci. 24, 623–631.

Cao, Q.L., Zhang, Y.P., Howard, R.M., Walters, W.M., Tsoulfas, P., Whittemore, S.R., 2001. Pluripotent stem cells engrafted into the normal or lesioned adult rat spinal cord are restricted to a glial lineage. Exp. Neurol. 167, 48–58.

Cummings, B.J., Uchida, N., Tamaki, S.J., Salazar, D.L., Hooshmand, M., Summers, R., Gage, F.H., Anderson, A.J., 2005. Human neural stem cells differentiate and promote locomotor recovery in spinal cord-injured mice. Proc. Natl. Acad. Sci. U. S. A. 102, 14069–14074.

Duffy, P., Wang, X., Siegel, C.S., Tu, N., Henkemeyer, M., Cafferty, W.B., Strittmatter, S.M., 2012. Myelin-derived ephrinB3 restricts axonal regeneration and recovery after adult CNS injury. Proc. Natl. Acad. Sci. U. S. A. 109, 5063–5068.

Fleming, J.C., Norenberg, M.D., Ramsay, D.A., Dekaban, G.A., Marcillo, A.E., Saenz, A.D., Pasquale-Styles, M., Dietrich, W.D., Weaver, L.C., 2006. The cellular inflammatory response in human spinal cords after injury. Brain 129, 3249–3269.

Gomi, M., Aoki, T., Takagi, Y., Nishimura, M., Ohsugi, Y., Mihara, M., Nozaki, K., Hashimoto, N., Miyamoto, S., Takahashi, J., 2011. Single and local blockade of interleukin-6 signaling promotes neuronal differentiation from transplanted embryonic stem cell-derived neural precursor cells. J. Neurosci. Res. 89, 1388–1399.

Heishi, M., Ichihara, J., Teramoto, R., Itakura, Y., Hayashi, K., Ishikawa, H., Gomi, H., Sakai, J., Kanaoka, M., Taiji, M., Kimura, T., 2006. Global gene expression analysis in liver of obese diabetic db/db mice treated with metformin. Diabetologia 49, 1647–1655.

Ikegami, T., Nakamura, M., Yamane, J., Katoh, H., Okada, S., Iwanami, A., Watanabe, K., Ishii, K., Kato, F., Fujita, H., Takahashi, T., Okano, H.J., Toyama, Y., Okano, H., 2005. Chondroitinase ABC combined with neural stem/progenitor cell transplantation enhances graft cell migration and outgrowth of growth-associated protein-43-positive fibers after rat spinal cord injury. Eur. J. Neurosci. 22, 3036–3046.

Iwanami, A., Yamane, J., Katoh, H., Nakamura, M., Momoshima, S., Ishii, H., Tanioka, Y., Tamaoki, N., Nomura, T., Toyama, Y., Okano, H., 2005. Establishment of graded spinal cord injury model in a nonhuman primate: the common marmoset. J. Neurosci. Res. 80, 172–181.

Kitamura, K., Fujiyoshi, K., Yamane, J., Toyota, F., Hikishima, K., Nomura, T., Funakoshi, H., Nakamura, T., Aoki, M., Toyama, Y., Okano, H., Nakamura, M., 2011. Human hepatocyte growth factor promotes functional recovery in primates after spinal cord injury. PLoS One 6, e27706.

Kobayashi, Y., Okada, Y., Itakura, G., Iwai, H., Nishimura, S., Yasuda, A., Nori, S., Hikishima, K., Konomi, T., Fujiyoshi, K., Tsuji, O., Toyama, Y., Yamanaka, S., Nakamura, M., Okano, H., 2012. Pre-evaluated safe human iPSC-derived neural stem cells promote functional recovery after spinal cord injury in common marmoset without tumorigenicity. PLoS One 7, e52787.

Kubota, K., Saiwai, H., Kumamaru, H., Maeda, T., Ohkawa, Y., Aratani, Y., Nagano, T., Iwamoto, Y., Okada, S., 2012. Myeloperoxidase exacerbates secondary injury by generating highly reactive oxygen species and mediating neutrophil recruitment in experimental spinal cord injury. Spine (Phila Pa 1976) 37, 1363–1369.

Kumamaru, H., Ohkawa, Y., Saiwai, H., Yamada, H., Kubota, K., Kobayakawa, K., Akashi, K., Okano, H., Iwamoto, Y., Okada, S., 2012. Direct isolation and RNA-seq reveal environment-dependent properties of engrafted neural stem/progenitor cells. Nat. Commun. 3, 1140.

Kumamaru, H., Kobayakawa, K., Saiwai, H., Kubota, K., Yokota, K., Ohkawa, Y., Shiba, K., Iwamoto, Y., Okada, S., 2013. The therapeutic activities of engrafted neural stem/precursor cells are not dormant in the chronically injured spinal cord. Stem Cells 31, 1535–1547.

Langmead, B., Trapnell, C., Pop, M., Salzberg, S.L., 2009. Ultrafast and memory-efficient alignment of short DNA sequences to the human genome. Genome Biol. 10, R25.

Lee, J.Y., Kim, H.S., Choi, H.Y., Oh, T.H., Ju, B.G., Yune, T.Y., 2012a. Valproic acid attenuates blood–spinal cord barrier disruption by inhibiting matrix metalloprotease-9 activity and improves functional recovery after spinal cord injury. J. Neurochem. 121, 818–829.

Lee, J.Y., Kim, H.S., Choi, H.Y., Oh, T.H., Yune, T.Y., 2012b. Fluoxetine inhibits matrix metalloprotease activation and prevents disruption of blood–spinal cord barrier after spinal cord injury. Brain 135, 2375–2389.

Llorens, F., Hummel, M., Pastor, X., Ferrer, A., Pluvinet, R., Vivancos, A., Castillo, E., Iraola, S., Mosquera, A.M., Gonzalez, E., Lozano, J., Ingham, M., Dohm, J.C., Noguera, M., Kofler, R., del Rio, J.A., Bayes, M., Himmelbauer, H., Sumoy, L., 2011. Multiple platform assessment of the EGF dependent transcriptome by microarray and deep tag sequencing analysis. BMC Genomics 12, 326.

Lu, P., Wang, Y., Graham, L., McHale, K., Gao, M., Wu, D., Brock, J., Blesch, A., Rosenzweig, E.S., Havton, L.A., Zheng, B., Conner, J.M., Marsala, M., Tuszynski, M.H., 2012. Long-distance growth and connectivity of neural stem cells after severe spinal cord injury. Cell 150, 1264–1273.

Matsui, T., Takano, M., Yoshida, K., Ono, S., Fujisaki, C., Matsuzaki, Y., Toyama, Y., Nakamura, M., Okano, H., Akamatsu, W., 2012. Neural stem cells directly differentiated from partially reprogrammed fibroblasts rapidly acquire gliogenic competency. Stem Cells 30, 1109–1119.

Mortazavi, A., Williams, B.A., McCue, K., Schaeffer, L., Wold, B., 2008. Mapping and quantifying mammalian transcriptomes by RNA-Seq. Nat. Methods 5, 621–628.

Mukaino, M., Nakamura, M., Yamada, O., Okada, S., Morikawa, S., Renault-Mihara, F., Iwanami, A., Ikegami, T., Ohsugi, Y., Tsuji, O., Katoh, H., Matsuzaki, Y., Toyama, Y., Liu, M., Okano, H., 2010. Anti-IL-6-receptor antibody promotes repair of spinal cord injury by inducing microglia-dominant inflammation. Exp. Neurol. 224, 403–414.

Nakamura, M., Houghtling, R.A., MacArthur, L., Bayer, B.M., Bregman, B.S., 2003. Differences in cytokine gene expression profile between acute and secondary injury in adult rat spinal cord. Exp. Neurol. 184, 313–325.

Nishimura, S., Yasuda, A., Iwai, H., Takano, M., Kobayashi, Y., Nori, S., Tsuji, O., Fujiyoshi, K., Ebise, H., Toyama, Y., Okano, H., Nakamura, M., 2013. Time-dependent changes in the microenvironment of injured spinal cord affects the therapeutic potential of neural stem cell transplantation for spinal cord injury. Mol. Brain 6, 3.

Noble, L.J., Donovan, F., Igarashi, T., Goussev, S., Werb, Z., 2002. Matrix metalloproteinases limit functional recovery after spinal cord injury by modulation of early vascular events. J. Neurosci. 22, 7526–7535.

Nori, S., Okada, Y., Yasuda, A., Tsuji, O., Takahashi, Y., Kobayashi, Y., Fujiyoshi, K., Koike, M., Uchiyama, Y., Ikeda, E., Toyama, Y., Yamanaka, S., Nakamura, M., Okano, H., 2011. Grafted human-induced pluripotent stem-cell-derived neurospheres promote motor functional recovery after spinal cord injury in mice. Proc. Natl. Acad. Sci. U. S. A. 108, 16825–16830.

Ogawa, Y., Sawamoto, K., Miyata, T., Miyao, S., Watanabe, M., Nakamura, M., Bregman, B.S., Koike, M., Uchiyama, Y., Toyama, Y., Okano, H., 2002. Transplantation of in vitro-expanded fetal neural progenitor cells results in neurogenesis and functional recovery after spinal cord contusion injury in adult rats. J. Neurosci. Res. 69, 925–933.

Okada, S., Nakamura, M., Mikami, Y., Shimazaki, T., Mihara, M., Ohsugi, Y., Iwamoto, Y., Yoshizaki, K., Kishimoto, T., Toyama, Y., Okano, H., 2004. Blockade of interleukin-6 receptor suppresses reactive astrogliosis and ameliorates functional recovery in experimental spinal cord injury. J. Neurosci. Res. 76, 265–276.

Okada, S., Ishii, K., Yamane, J., Iwanami, A., Ikegami, T., Katoh, H., Iwamoto, Y., Nakamura, M., Miyoshi, H., Okano, H.J., Contag, C.H., Toyama, Y., Okano, H., 2005. In vivo imaging of engrafted neural stem cells: its application in evaluating the optimal timing of transplantation for spinal cord injury. FASEB J. 19, 1839–1841.

Okano, H., 2002. Stem cell biology of the central nervous system. J. Neurosci. Res. 69, 698–707.

Okano, H., Nakamura, M., Yoshida, K., Okada, Y., Tsuji, O., Nori, S., Ikeda, E., Yamanaka, S., Miura, K., 2013. Steps toward safe cell therapy using induced pluripotent stem cells. Circ. Res. 112, 523–533.

Popovich, P.G., Wei, P., Stokes, B.T., 1997. Cellular inflammatory response after spinal cord injury in Sprague–Dawley and Lewis rats. J. Comp. Neurol. 377, 443–464.

Saldanha, A.J., 2004. Java Treeview—extensible visualization of microarray data. Bioinformatics 20, 3246–3248.

Shimada, H., Okada, Y., Ibata, K., Ebise, H., Ota, S., Tomioka, I., Nomura, T., Maeda, T., Kohda, K., Yuzaki, M., Sasaki, E., Nakamura, M., Okano, H., 2012. Efficient derivation of multipotent neural stem/progenitor cells from non-human primate embryonic stem cells. PLoS One 7, e49469.

Silver, J., Miller, J.H., 2004. Regeneration beyond the glial scar. Nat. Rev. Neurosci. 5, 146–156.

Tomioka, I., Maeda, T., Shimada, H., Kawai, K., Okada, Y., Igarashi, H., Oiwa, R., Iwasaki, T., Aoki, M., Kimura, T., Shiozawa, S., Shinohara, H., Suemizu, H., Sasaki, E., Okano, H., 2010. Generating induced pluripotent stem cells from common marmoset (*Callithrix jacchus*) fetal liver cells using defined factors, including Lin28. Genes Cells 15, 959–969.

Trapnell, C., Pachter, L., Salzberg, S.L., 2009. TopHat: discovering splice junctions with RNA-Seq. Bioinformatics 25, 1105–1111.

Tsuji, O., Miura, K., Okada, Y., Fujiyoshi, K., Mukaino, M., Nagoshi, N., Kitamura, K., Kumagai, G., Nishino, M., Tomisato, S., Higashi, H., Nagai, T., Katoh, H., Kohda, K., Matsuzaki, Y., Yuzaki, M., Ikeda, E., Toyama, Y., Nakamura, M., Yamanaka, S., Okano, H., 2010. Therapeutic potential of appropriately evaluated safe-induced pluripotent stem cells for spinal cord injury. Proc. Natl. Acad. Sci. U. S. A. 107, 12704–12709.

Tuszynski, M.H., Gabriel, K., Gage, F.H., Suhr, S., Meyer, S., Rosetti, A., 1996. Nerve growth factor delivery by gene transfer induces differential outgrowth of sensory, motor, and noradrenergic neurites after adult spinal cord injury. Exp. Neurol. 137, 157–173.

Wang, Z., Gerstein, M., Snyder, M., 2009. RNA-Seq: a revolutionary tool for transcriptomics. Nat. Rev. Genet. 10, 57–63.

Xiong, Y., Rabchevsky, A.G., Hall, E.D., 2007. Role of peroxynitrite in secondary oxidative damage after spinal cord injury. J. Neurochem. 100, 639–649.

Zhang et al. Molecular Brain 2014, 7:14
http://www.molecularbrain.com/content/7/1/14

Molecular Brain

RESEARCH Open Access

Rewiring of regenerated axons by combining treadmill training with semaphorin3A inhibition

Liang Zhang[1,2,3†], Shinjiro Kaneko[1,4†], Kaoru Kikuchi[5], Akihiko Sano[5], Miho Maeda[5], Akiyoshi Kishino[5], Shinsuke Shibata[2], Masahiko Mukaino[3], Yoshiaki Toyama[1], Meigen Liu[3], Toru Kimura[5], Hideyuki Okano[2*†] and Masaya Nakamura[1*†]

Abstract

Background: Rats exhibit extremely limited motor function recovery after total transection of the spinal cord (SCT). We previously reported that SM-216289, a semaphorin3A inhibitor, enhanced axon regeneration and motor function recovery in SCT adult rats. However, these effects were limited because most regenerated axons likely do not connect to the right targets. Thus, rebuilding the appropriate connections for regenerated axons may enhance recovery. In this study, we combined semaphorin3A inhibitor treatment with extensive treadmill training to determine whether combined treatment would further enhance the "rewiring" of regenerated axons. In this study, which aimed for clinical applicability, we administered a newly developed, potent semaphorin3A inhibitor, SM-345431 (Vinaxanthone), using a novel drug delivery system that enables continuous drug delivery over the period of the experiment.

Results: Treatment with SM-345431 using this delivery system enhanced axon regeneration and produced significant, but limited, hindlimb motor function recovery. Although extensive treadmill training combined with SM-345431 administration did not further improve axon regeneration, hindlimb motor performance was restored, as evidenced by the significant improvement in the execution of plantar steps on a treadmill. In contrast, control SCT rats could not execute plantar steps at any point during the experimental period. Further analyses suggested that this strategy reinforced the wiring of central pattern generators in lumbar spinal circuits, which, in turn, led to enhanced motor function recovery (especially in extensor muscles).

Conclusions: This study highlights the importance of combining treatments that promote axon regeneration with specific and appropriate rehabilitations that promote rewiring for the treatment of spinal cord injury.

Keywords: Axonal regeneration, Semaphorin3A, Inhibitor, Rehabilitation, Rewiring, Drug delivery system

Background

Severe spinal cord injuries (SCI) in adult mammals result in various deficits throughout life. The limited capability of axons to regenerate in the central nervous system (CNS) is thought to be the main reason for these lasting deficits. Previous studies have suggested that both extrinsic and intrinsic factors in the CNS contribute to this incapacity for axonal regeneration [1-4]. Several distinct extrinsic molecules have been proposed to hinder axonal regeneration, including CNS myelin-associated proteins (MAG, Nogo, OMgp) [5-9], chondroitin sulphate proteoglycans [10,11], semaphorin3A [12,13] and RGM (repulsive guidance molecule) [14,15]. Neutralizing one (or several) of these molecules enhances axonal regeneration and results in some degree of functional recovery [10,16,17]. Until recently, it remained unknown whether neutralizing semaphorin3A would also lead to axonal regeneration and motor function recovery, in part because semaphorin3A deficiency is lethal [18]. Thus, we previously developed a selective and potent semaphorin3A inhibitor called SM-216289 [19] that selectively inhibits semaphorin3A signaling both *in vitro* and *in vivo* [20]. Administration of SM-216289 to adult rats after total spinal cord transection

* Correspondence: hidokano@a2.keio.jp; masa@a8.keio.jp
†Equal contributors
[2]Department of Physiology, Keio University School of Medicine, 35 Shinanomachi, Shinjuku, Tokyo 160-8582, Japan
[1]Department of Orthopedic Surgery, Keio University School of Medicine, 35 Shinanomachi, Shinjuku, Tokyo 160-8582, Japan
Full list of author information is available at the end of the article

(SCT) led to axonal regeneration and motor function recovery [20]. In addition, axonal regeneration and functional recovery have now been observed after several treatments that block 1 or more axonal growth inhibitors (including SM-216289). However, these effects are moderate at best, presumably because most of the regenerated axons do not connect with the correct targets [21]. Thus, rebuilding the appropriate connections of regenerated axons in lesioned spinal cords remains an important unresolved issue.

Body weight-supported treadmill training induces plastic changes in lesioned spinal cords and is useful for maximizing residual locomotor function after moderate SCI [22,23]. Furthermore, even after severe SCI, treadmill training partially improves hindlimb coordination [24] by inducing plasticity in specific spinal locomotor circuits called "central pattern generators" (CPGs). More specifically, these plastic changes have been shown to result in the recovery of plantar step walking in cats [25] and neonatal rats [26]. Furthermore, SCT adult rats partially recover plantar step walking when treadmill training is combined with other appropriate treatments, such as epidural electrical stimulation [27], pharmacological treatments [24] or cell transplantation [28]. Thus, with specific and appropriate rehabilitation, spinal cord CPGs can be reorganized, and functionally appropriate connections between CPGs and regenerated (or residual) axons can be rebuilt. Therefore, we hypothesized that extensive treadmill training would assist in the correct wiring of axons regenerated by semaphorin3A inhibitor treatment and that this rewiring may contribute to further motor functional recovery after SCT.

However, several issues, including drug delivery, remain to be resolved before semaphorin3A inhibitors can be used in the clinic. In an attempt to resolve these issues, we developed a novel selective semaphorin3A inhibitor, SM-345431 (Vinaxanthone), which demonstrates physicochemical properties equivalent to those of SM-216289 but also improvements that should allow for the development of a higher quality pharmaceutical product. Additionally, we developed a novel drug delivery system (DDS) utilizing a silicone sheet. With future clinical applications in mind, we chose to evaluate SM-345431 with this novel DDS. We observed that, consistent with our previous study [20], SM-345431 treatment enhanced axon regeneration and resulted in significant, but limited, hindlimb motor function recovery. Although extensive treadmill training with SM-345431 administration did not further improve axon regeneration, hindlimb motor performance was restored, as evidenced by the execution of plantar steps on a treadmill using a body support system (BSS). Moreover, immunohistological analysis suggested that SM-345431 administration with treadmill training reinforced the wiring of CPGs in lumbar spinal circuits and led to enhanced motor function recovery, especially in extensor muscles.

Results

Evaluation of a novel DDS and the activity of SM-345431 *in vitro*

In our previous study, we used an osmotic mini-pump to deliver the semaphorin3A inhibitor SM-216289 [20]. However, in clinical practice, this type of invasive drug delivery method is not ideal. Therefore, we developed a novel DDS that utilizes a silicone matrix to continuously deliver SM-345431 (a newly developed semaphorin3A inhibitor) intrathecally. We evaluated the drug release profile of SM-345431 in this new silicone matrix preparation and the potency of SM-345431-mediated semaphorin3A inhibition in vitro (Figure 1). SM-345431 exhibited semaphorin3A inhibiting activity with an IC50 of 0.1-0.2 μM in growth cone collapse assays using E8 chick and E14 rat dorsal root ganglia (DRG) (Figure 1A). When chick embryonic DRG explants and semaphorin3A-expressing COS7 cell aggregates (semaphorin3A-COS) were co-cultured in a collagen gel, the neurites of the DRG explants grew away from the semaphorin3A-COS, as shown in Figure 1B. However, when DRG explants and semaphorin3A-COS were co-cultured in the presence of SM-345431, radial extensions of the neurites were observed, which suggests that the chemo-repulsive effects of semaphorin3A were blocked by SM-345431 in a dose-dependent manner (Figure 1B). We also evaluated the selectivity of SM-345431 for semaphorin3A inhibition by examining the pharmacological profile of SM-345431 (Tables 1 and 2). As shown in these tables, the IC50 value for semaphorin3A inhibition was substantially lower than the other IC50s, which suggested that SM-345431 is a highly selective semaphorin3A inhibitor. To examine the semaphorin3A inhibiting activity of SM-345431 while it was being released from the silicone matrix (SM-345431-silicone), 1 mg of a silicone sheet containing 100 μg SM-345431 was placed into collagen gel cultures containing DRG explants and semaphorin3A-COS (Figure 1C). Assuming that 5% of the SM-345431 was released and uniformly diffused throughout the culture during the 2 days of incubation, the final concentration of SM-345431 was approximately 5 μM, which is a large enough dose to inhibit semaphorin3A activity. Radial neurite extension was observed in cultures with SM-345431-silicone but not in those with control silicone, indicating that semaphorin3A activity had been inhibited by SM-345431. We also measured the cumulative percentage of released doses of SM-345431 using this DDS over 2 months *in vitro* (Figure 1E) and found that this DDS released a constant dose of SM-345431 and was stable *in vitro*. When 7 mm × 5 mm × 0.3 mm sheets were used, the amount of drug release stabilized at approximately 10 μg/day after an initial peak of drug release that occurred over the first 2 days (Figure 1F). For the *in vivo* study, we trimmed the silicone sheet into 3 mm × 3 mm × 0.3 mm pieces to fit the injury site following SCT (Figure 1G-I).

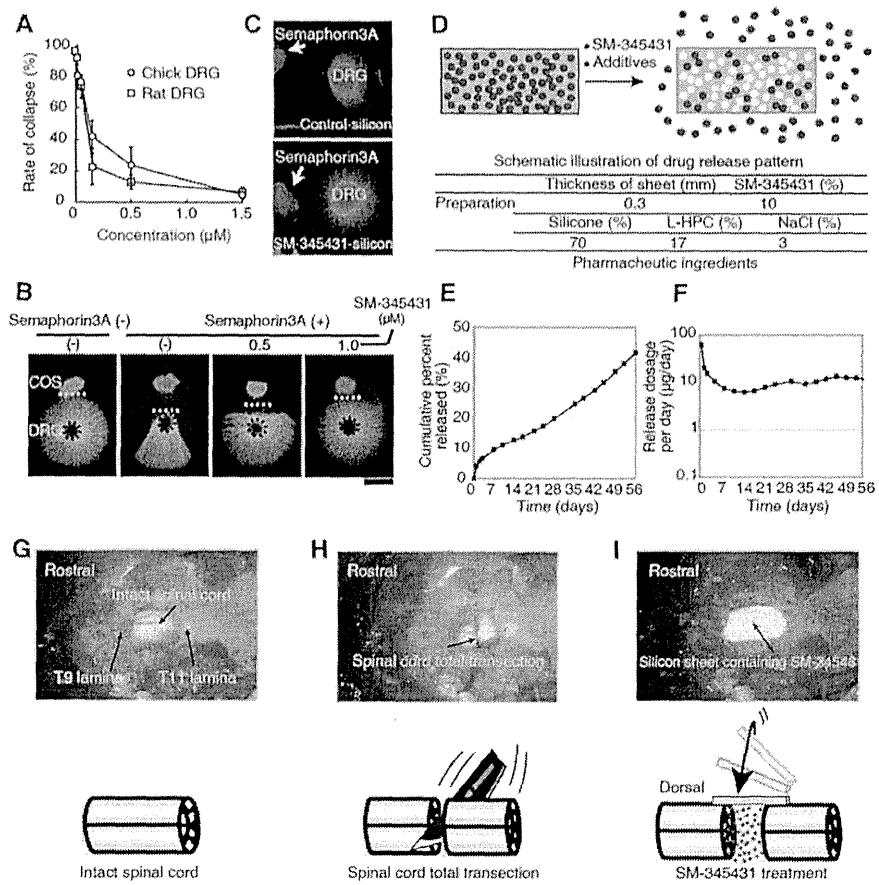

Figure 1 Preparation of the SM-345431 silicone DDS and *in vitro* release study. **(A)** Analysis of the inhibitory activity of SM-345431 in the growth cone collapse assay using E8 chick and E14 rat DRGs. **(B)** Collagen co-culture assay using E8 chick DRGs and semaphorin3A-expressing COS7 cell aggregates. **(C)** Pictures showing the effects of SM-345431-silicone or control-silicone in the collagen gel. **(D)** Schematic illustration of drug release from the matrix silicone preparation; the drug is dissolved in water, permeates into the preparation and is then released. The rate of water permeation into the silicone matrix is controlled by various additives, and the proportions of these additives included in the DDS control the variations in the drug release profile. The preparation used here contained the water-soluble additives listed in the table **(D)**. Stable and linear release of SM-345431 was observed for up to 2 months as shown in **(E)** and **(F)**. **(E, F)** SM-345431 release curve for the preparation. The linear cumulative percent release curve at 2 months **(E)** and the stable release dosage per day **(F)** are shown for the administration of SM-345431 using this novel DDS. **(G)** Exposed intact spinal cord. **(H)** Transected spinal cord. **(I)** The novel DDS we employed. A silicone sheet containing SM-345431 was placed onto the transected site of the spinal cord. The system allowed for stable and continuous release of the semaphorin3A inhibitor throughout the experimental period.

The release of SM-345431 (0.1 mg/mg loading 10%) *in vivo* was calculated as 0.5-0.7 μg/day, and this dose was similar to the dose of the semaphorin3A inhibitor (SM-216289) [19] that we administered using osmotic mini pumps in our previous study [20]. Therefore, the newly developed DDS allowed stable and continuous release of the newly developed, potent semaphorin3A inhibitor SM-345431.

SM-345431 delivery via the novel DDS enhanced axonal regeneration

To examine the regeneration of axons after SM-345431 treatment and SM-345431 treatment combined with extensive treadmill training, we evaluated axons in the injured spinal cord with immunostaining using antibodies against GAP43 and serotonin (5-HT) (Figure 2), GAP43 is widely used as a marker for regenerated axons. In both treatment groups, a marked increase in the number of GAP43-positive axons was observed at the epicenter of the injury (Figure 2D-F) and in the surrounding area (Figure 2G-I). Compared with the control group, the number of GAP43 axons was significantly increased in both the SM-345431 treatment group and the combined treatment group, especially at 1 mm caudal to the injury epicenter (Figure 2J). No significant difference was observed between the 2 treatment groups. Thus, administration of the semaphorin3A inhibitor SM-345431 using this DDS enhanced axonal

Table 1 Pharmacological profile of SM-345431 (part 1)

Enzymes	IC50 (μm)
Semaphorin	0.1-0.2
Matrix Metalloproteinase-1 (MMP-1)	>10
Matrix Metalloproteinase-7 (MMP-7)	10
Matrix Metalloproteinase-2 (MMP-2)	>10
Matrix Metalloproteinase-3 (MMP-3)	>10
Matrix Metalloproteinase-9 (MMP-9)	>10
Phospholipase PLA2-1	>10
Phospholipase PLC	>10
Caspase 1	>10
Caspase 3	>10
Caspase 6	>10
Caspase 7	>10
Caspase 8	>10
Protein Tyrosine Phosphatase, CD45	>10
Protein Tyrosine Phosphatase, PTP1B	>10
Protein Tyrosine Phosphatase, PTP1C	>10
Protein Tyrosine Phosphatase, T-Cell	>10
Sphingomyelinase, Neutral (N-SMase)	>10
Chemokine CCR1	>10
Chemokine CCR2B	>10
Chemokine CCR4	>10
Chemokine CCR5	>10
Chemokine CXCR2 (IL-8B)	>10
Glucocorticoid	>10
Interleukin IL-1	>10
Interleukin IL-2	>10
Interleukin IL-6	>10
Tumor Necrosis Factor (TNF), Non-selective	>10
Adhesion, fibronectin-mediated	>10
Adhesion, ICAM-1-Mediated	>10
Adhesion, VCAM-1-Mediated	>10
Cell proliferation, B-Cell+LPS	>10
Cell proliferation, T-Cell+Con A	>10
Mediator release, IL-1beta	>10
Mediator release, IFN-gamma	>10
Mediator release, IL-10	>10
Mediator release, IL-2	>10
Mediator release, IL-4	>10
Mediator release, IL-5	>10
Mediator release, IL-6	>10
Mediator release, TNF-alfa, PBML	>10
Transcription response, NF-AT	>10
Transcription response, NF-kB	>10

Summary of the IC50 values for binding assays of various receptors and ion channels, and IC50 values for the inhibition of various enzymes. The IC50 value for semaphorin3A inhibition was extremely low compared to that of the other factors.

Table 2 Pharmacological profile of SM-345431 (part 2)

Kinases	IC50 (μm)
CaMKII	>10
CDK5/p35	>10
cSRC	>10
EGFR	0.90
EphA2	>10
EphA4	0.80
EphB2	0.68
EphB4	>10
Fes	>10
FGFR1	>10
FGFR2	>10
FGFR3	0.77
FGFR4	0.64
Flt1	>10
Flt3	>10
Fyn	>10
GSK3α	2.46
GSK3β	>10
IGF-1R	>10
JAK3	>10
KDR	>10
MAPK2	>10
MEK1	>10
MEK4	>10
MKK6	>10
PAK2	>10
PAK4	>10
PKA	>10
PKBα	>10
PKBβ	>10
PKCγ	>10
ROCK-I	>10
ROCK-II	>10
ROCK-II	>10
SAPK2a	>10
TrkA	>10
TrkB	>10
PI 3-Kγ	>10

Summary of the IC50 values revealed by inhibition tests for various kinases. The data in Tables 1 and 2 suggest that SM-345431 was highly selective for semaphorin3A inhibition.

regeneration. However, no additional axonal regeneration was observed when SM-345431 treatment was combined with treadmill training.

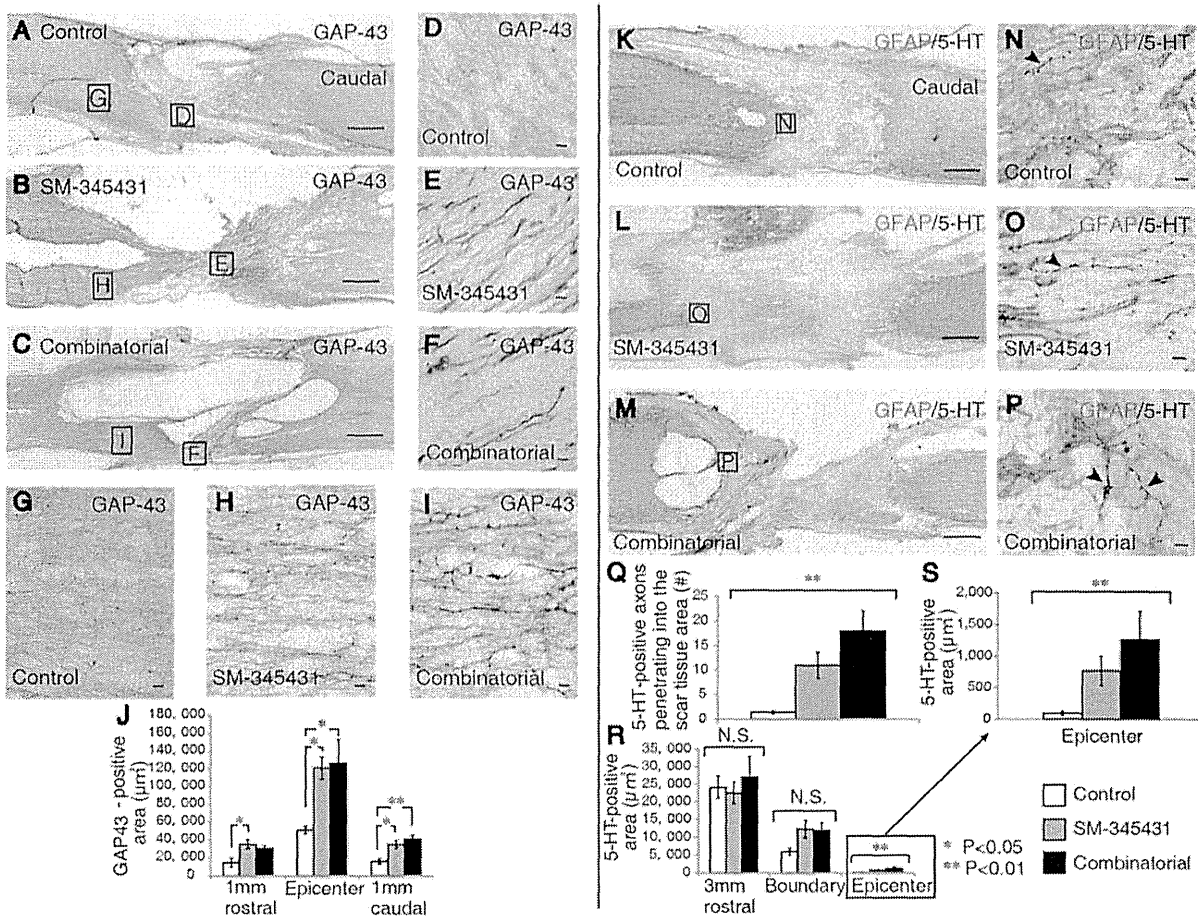

Figure 2 SM-345431 enhanced axonal regeneration *in vivo*, but combined treatment had only a limited effect on further axon regeneration. (A-I) Sagittal sections from SCT rats immunostained for GAP-43. Low-magnification images of the control **(A)**, SM-345431 **(B)** and combined treatment **(C)** groups. Scale bars = 500 μm. **(D-F)** Magnified images of the boxed areas shown in **A-C**. Scale bars = 10 μm. **(G-I)** Additional magnified images of the boxed areas shown in **A-C**. Scale bars = 10 μm. **(J)** Quantitative analysis of GAP-43-positive areas at 1 mm rostral to the lesion, 1 mm caudal to the lesion and at the epicenter of the lesion. Immunohistochemistry was performed using DAB with nickel enhancement. *P < 0.05, **P < 0.01. Statistical analyses were performed using one-way ANOVA and Bonferroni post hoc tests. Data are represented as the mean ± S.E.M. **(K-P)** Sagittal sections of SCT rats double-stained for 5-HT and GFAP. Scar tissue is outlined by GFAP staining, which also allowed for confirmation of total transection of the spinal cord in each animal. **(K-M)** Low-magnification images of the control **(K)**, SM-345431 **(L)** and combined treatment **(M)** groups. Scale bars = 500 μm. **(N-P)** Magnified images of the boxed areas shown in **K-M**. Scale bars = 10 μm. Arrowheads represent 5-HT-positive (serotonergic) axons. **(Q-S)** Quantitative analyses of 5-HT-positive axons that penetrated into the scar tissue. **(Q)** Quantitative analysis of the number of 5-HT-positive axons that penetrated into the lesion site. **(R,S)** Quantitative analysis of the 5-HT-positive area within the scar tissue area. Immunohistochemistry was performed by double-staining using DAB with or without nickel enhancement. The left side is rostral in all images. **P < 0.01. Statistical analyses were performed using a Kruskal-Wallis H test. Data represent the mean ± S.E.M.

The raphespinal tract axons, which can be detected by immunohistochemistry against serotonin (5-HT), contribute to functional locomotor control, and regeneration of these axons leads to substantial enhancement of motor function recovery [28]. Therefore, we also evaluated the regeneration of raphespinal tract axons using a GFAP antibody to delineate scar tissue at the injury site and a 5-HT antibody to visualize raphespinal axons. In control animals, 5-HT-positive axons were restricted to the area rostral to the transected site, and few 5HT-positive axons entered the GFAP-negative scar tissue area (Figure 2K,N). Interestingly, significantly more 5-HT-positive axons penetrated the GFAP-negative scar tissue area after SM-345431 treatment and combined treatment as compared to the control conditions (Figure 2K-S). Because we used a total transection model in this study, the 5-HT-positive axons that penetrated the GFAP-negative scar tissue in the treatment groups were regarded as regenerated axons (Figure 2L-P). Cortico-spinal tract (CST) axons are known to be incapable of regeneration after transection, even